SYNTHESIS OF ZIF-67-rGO-Mn_xO_y BASED HYBRID MOF ELECTRODE MATERIAL FOR HIGH-PERFORMANCE SUPERCAPACITOR

By

SANJIDA AFRIN

In the partial fulfillment of the requirement for the degree

of

MASTER OF PHILOSOPHY IN CHEMISTRY

Department of Chemistry

BANGLADESH UNIVERSITY OF ENGINEERING AND TECHNOLOGY (BUET),

DHAKA-1000

December 2022

Bangladesh University of Engineering and Technology (BUET), Dhaka-1000
Department of Chemistry

Certification of Thesis
A thesis on

SYNTHESIS OF ZIF-67-rGO-Mn_xO_y BASED HYBRID MOF ELECTRODE MATERIAL FOR HIGH-PERFORMANCE SUPERCAPACITOR

By
Sanjida Afrin

Roll No.: 0419033603, Session: April 2019, has been accepted as satisfactory in partial fulfillment of the requirements for the degree of Master of Philosophy (M.Phil.) in Chemistry and certify that the student has demonstrated satisfactory knowledge of the field covered by this thesis in an oral examination held on December 14, 2022.

Board of Examiners

1. Dr. Md. Shakhawat Hossain Firoz
Professor
Department of Chemistry
BUET, Dhaka-1000.

Supervisor & Chairman

2. Prof. Al-Nakib Chowdhury
Professor and Head
Department of Chemistry
BUET, Dhaka-1000

Member (Ex-officio)

3. Dr. Abu Bin Imran
Associate Professor
Department of Chemistry
BUET, Dhaka-1000

Member

4. Dr. Chanchal Kumar Roy
Assistant Professor
Department of Chemistry
BUET, Dhaka-1000

Member

5. Dr. Muhammed Shah Miran
Professor
Department of Chemistry
University of Dhaka, Dhaka -1000

Member (External)

CANDIDATE'S DECLARATION

It is hereby declared that this thesis or any part of it has not been submitted elsewhere for the award of any degree or diploma.

Sanjida Afrin

Sanjida Afrin

DEDICATION

I dedicate this thesis to my beloved junior late Kazi Rifat Mamun (1995-2019).

Kazi Rifat Mamun was an M.Sc student of the Department of Chemistry, BUET (April-2019) session. In late 2019, Rifat died of Guillain-Barré syndrome (GBS).

He completed his B.Sc degree in Chemistry from Khulna University in 2019. Rifat was a talented young star and dedicated person who involved himself in fundamental research. He was a very brilliant, polite, and innocent person I have ever seen. May Allah grant his soul and award him Jannah.

He came along with us to get himself enrolled in the M.Sc program. They were passing their life with tremendous joy and happiness together. It is suspected that Rifat got ill after consuming contaminated water or food. But, in reality, the exact reason for GBS is yet unknown.

Acknowledgment

At the outset, I respectfully express my heartfelt appreciation to the almighty, the most gracious, benign, and compassionate founder, for the immeasurable kindness given to me in carrying out the study effort provided in the degree. I would like to express my sincere gratitude and appreciation to my honorable teacher and supervisor, Dr. Md. Shakhawat Hossain Firoz, Professor, Department of Chemistry, Bangladesh University of Engineering and Technology (BUET), for his considerate supervision, vital guidance, valuable and constructive suggestions, liberal assistance, and unending support throughout the entire duration. His efforts and attributed work have tremendously influenced who I am now. Being a member of his ambitious research team is a real blessing for me. I would like to express my heartfelt gratitude to Dr. Chanchal Kumar Roy and Dr. Al Nakib Chowdhury for their invaluable recommendations, opinions, and assistance during the research period. I appreciate the help I occasionally receive from the other reputable chemistry lecturers at BUET. For their constant assistance during my academic years, I also like to thank the officials and employees of the Department of Chemistry at BUET. I sincerely appreciate the board of examiners' informative opinions and helpful suggestions. Special thanks to Md. Yeasin Arafat Tarek, Ragib Shakil, Md. Akter Hossain Reaz for their continuous help during the research.

I am also thankful to other fellows of the Chemistry Materials Laboratory for their cooperation during the research period. I am grateful to the authority of BUET and the Ministry of Education for their financial support in this research. Finally, I would like to express my heartfelt indebtedness and profound gratitude to my beloved father, mother, husband, and family members for their continuous inspiration and immeasurable sacrifices throughout my study.

November 2022 Sanjida afrin

GRAPHICAL ABSTRACT

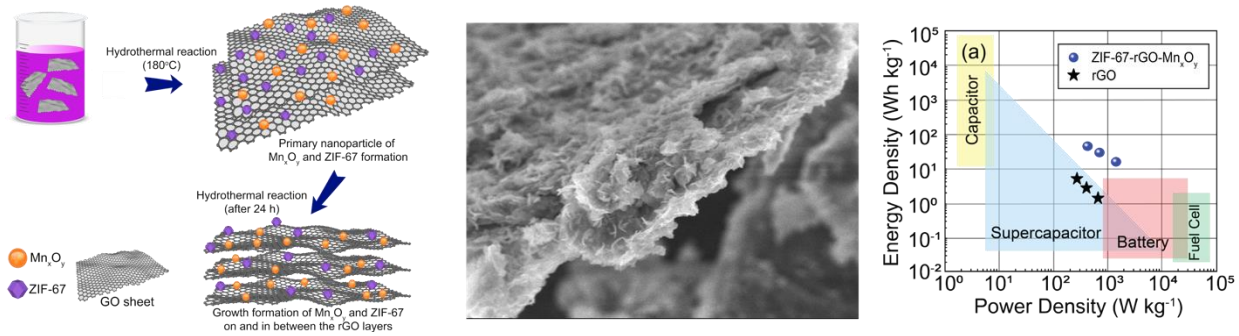

ABSTRACT

This research work has established a simple hydrothermal reaction-based synthesis of hybrid material, ZIF-67-rGO-Mn_xO_y. Using 0.5M Na_2SO_4, the electrochemical investigation of this hybrid material was made in order to evaluate the supercapacitor performance. Due to the self-oriented conductive rGO layers with expanded interlayer distance and hydrothermally grown ZIF-67, Mn_xO_y into the surface of rGO, it exhibits relatively high surface area and well-defined corn-flakes morphology. ZIF-67 is added into the rGO layer for the conductivity increase and Mn_xO_y is added into rGO layer and for the multivalent state of Mn it influences the redox reaction in between them. With an energy density of 31 Whkg^{-1} at 1 Ag^{-1} current density, the synergistic impact of ZIF-67, and Mn_xO_y in between the rGO layers, the hybrid material exhibits dramatically increased specific capacitance of 457 Fg^{-1}. Additionally, the hybrid material based on ZIF-67-rGO-Mn_xO_y demonstrated a satisfactory power density of 350 Wkg^{-1}. The solution resistance (R_s) for ZIF-67-rGO-Mn_xO_y was found 2.3 Ω and after 10000 cycles, the capacity retention was 97% of the initial value.

KEYWORDS: *Hybrid Supercapacitor, Gel formation, ZIF-67-rGO-Mn_xO_y, ternary hybrid.*

Table of Contents

Figures

Tables

List of Abbreviations of Technical Symbols and Terms

1. GO – Graphene Oxide
2. rGO – Reduced graphene oxide
3. C_{sp} – Specific capacitance
4. E – Energy density
5. P – Power density
6. i/m – Current density
7. ΔV – Potential difference
8. Δt – Discharging time
9. Hmim- 2-methylimidazol
10. ZIF- Zeolitic imidazolate framework
11. MOF- Metal organic framework

CHAPTER 1

INTRODUCTION

1.1 Introduction

Electricity is considered the greatest invention of human beings ever, and modern civilization is almost entirely dependent on electrical energy. Thus, over the few decades, the sustainable production of electricity has been heavily emphasized, and as a result, there are many technologies, such as nuclear fission reactors, hydroelectricity, solar panel, geothermal energy, etc., have been introduced as the solution to produce green electricity. The problems regarding fossil fuel burning and emissions to produce electricity seem to be resolved, but still, the vehicles on the road run by fossil fuel are a more significant concern towards energy and environmental security. Thus, finding an appropriate alternative to fossil fuels is urgent to reduce CO_2 and greenhouse gas emissions. Towards the solution, an induction engine run by electricity can be the only solution as the induction engine does not emit anything at all. The induction engine only requires a high-performing electrical energy storage device as its power supply. Thus today's material scientists are intensively focusing on the development of these energy storage devices. It is undoubtedly true that lithium-ion batteries (LiBs) are quite successful in this race and have shown tremendous performance in the commercial energy storage sector.[1] Those LiBs can store massive electrical energy and sufficiently supply charge for a longer period. But, the main problem with using LiBs or any other similar batteries in electric vehicles is their lower power density.[2] Whereas, high-performing electric vehicles mainly require an energy storage system with high energy and power density at a time. In brief, the terminology, 'energy density means the amount of electrical energy stored in an energy storage device, and power density means the speed to deliver this energy. Except for a few modern and hybrid battery systems, almost no battery system can provide this performance and the cost of fabrication of those modern hybrid batteries are still sky-high. This is continuously preventing the necessary advancement and sustainability in electric vehicle industries. Fortunately, supercapacitors (SCs) are the new dimension of energy storage devices that can provide high power density and optimum energy density at a time and are thus considered to bridge the gap between batteries and regular capacitors, a viable alternative for clean and renewable energy applications.[3] Besides, along with quick charged-discharge rates, SCs provide longer cycle life when compared to regular

capacitors and batteries with several uses in hybrid electric cars, particularly for regenerative brakes, strategic sectors, high-power UPS, and solar inverters.

However, the energy storage mechanism of a supercapacitor (SC) device is principally dependent upon two factors such as the electrode used during the fabrication of SC devices and the electrolytic system deployed. Most importantly, the whole electrical charge is stored in the electrode materials and this is why the available surface area, conductivity, and morphological orientation of those electrode materials are the priority in designing high-performing electrode materials. Based on the storage mechanism, the SC electrode materials are classified into three ways such as (i) electrical double-layer capacitors (EDLC), (ii) pseudocapacitors, and (ii) hybrid capacitors.[4] Carbonaceous materials such as reduced graphene oxide (rGO, pristine graphene, activated charcoal, activated carbon, etc. are the best for storing charge in the EDLC mechanism in an SC device. On the other hand, pseudocapacitors store charge by performing redox reactions in the presence of electrolytes and merely by forming EDLC.[5] Lastly, the hybrid materials are a combination of EDLC and pseudocapacitors and thus provide synergistic performance from both types of electrodes. As a result, hybrid electrodes are the best performing as those provide higher specific capacitance with high energy and power density as well as maintain longer cyclic stability. Now, toward the fabrication of hybrid electrodes, the selection of carbonaceous and pseudocapacitive materials is highly important as their morphological composition determines the performance of the SC system. However, rGO has become popular among all carbonaceous materials as EDLC electrodes due to its great surface area, accessibility, cheap cost, and improved processability.[6] Thus, the literature reports robust research on the rGO-based SC electrode fabrication. The problem regarding rGO is its lower energy density as it only stores charge in the EDLC mechanism.[7] Nowadays, it has been evident that when the rGO is intercalated with another pseudocapacitive material such as transitional metal oxides (TMOs), zeolitic imidazolate frameworks (ZIFs), or pure metal nanoparticles, the electrochemical performance becomes multiple times higher.[8] This occurs due to the deliberate redox reaction induced by the pseudocapacitors and enhancement in the interlayer distance of the rGO nanosheets.

The intercalation of these TMOs or ZIF thus can enhance the overall conductivity and charge storage capability in the hybrid materials, as they generate more accessible channels, pores, and

surface area for storing more electrical energy. Among so many ZIFs, ZIF-67 is special for its higher conductivity and pseudocapacitive performance.[9] Although the specific surface area provided by the ZIF-67 is very marginal, the cobalt existing in the ZIF-67 framework helps to build a conductive network with rGO layers. Besides, the expansion and distortion of rGO layers due to the intercalation of ZIF-67 facilitate enough scopes to store charge with a higher diffusion rate than alone rGO. But, still, the energy density of the ZIF-67-rGO composite remains lower as per the reports available in the literature.[10] It might be because of the inefficient intercalation of ZIF-67 into the rGO layers and the synthesis processes. Thus, one of the major tricks to developing an electrode material with higher energy density is to incorporate other TMOs in the existing composite. It has been seen that the incorporation of second pseudocapacitive material such as MnO_2, Mn_2O_3, Co_2O_3, Mn_xO_y, $Ni(OH)_2$ can always render the electrochemical performance by compensating the electrical response as well as providing a more accessible surface area, interconnected channels, and pores in the composite material.[11] Among all other TMOs, manganese oxides are considered the best source for use as pseudocapacitors in the formation of the hybrid composite due to their multiple oxidation states, availability, ease of preparation, etc.[12]

Herein, we reported a facile *in-situ* gel formation process for generating ZIF-67-rGO-Mn_xO_y ternary hybrid and fabricating a symmetrical high performing, practical SC device. The performance of an electrode material prepared via an *in-situ* process is always found to be favorable due to the possibility of greater intercalation of dopants in the substrates. Along with the synthesis process, the morphological and electrochemical characterization was also presented to evaluate the formation mechanism of the ternary hybrid and its charge storage mechanism. Besides, this study emphasized the use of neutral electrolytes such as sodium sulfate (Na_2SO_4) while the fabrication of the SC device. Usually, the performance of hybrid electrode materials gets enhanced when redox-active electrolytes (KOH, HCl, H_2SO_4) are employed,[13] but due to the abrupt and destructive redox reactions in the anode and cathode of the SC devices, the cyclic stability of the ternary hybrid become limited. Thus, keeping the Na_2SO_4 as an electrolyte, this study performed all the electrochemical tests with the newly synthesized ternary hybrid of ZIF-67-rGO-Mn_xO_y. To compare the difference in performance, pure ZIF-67, MnxOy, ZIF-67-Mn_xO_y, ZIF-67-rGO, and rGO-Mn_xO_y were also synthesized. Among all synthesized materials, the ternary hybrid of ZIF-67-rGO-Mn_xO_y has shown greater C_{sp}, higher power density with an

optimum energy density as well as maintained high cyclic stability. Thus it is expected that this synthesized ternary hybrid of ZIF-67-rGO-Mn_xO_y could be a prospective solution for the fabrication of real-time high-performing SC devices.

1.2 Objectives of Research

The specific objectives of this research are the

i. Synthesis of the Mn_xO_y, ZIF-67, binary ZIF-67- rGO, rGO-Mn_xO_y composite, and incorporation of the ZIF-67 as well as Mn_xO_y into the rGO to form ZIF-67-rGO-Mn_xO_y by in-situ preparation method.

ii. Investigation of the electrochemical performance of Mn_xO_y, ZIF-67, ZIF-67- rGO, rGO-Mn_xO_y, and ZIF-67-rGO-Mn_xO_y by performing Cyclic Voltammetry (CV), Galvanostatic Charging Discharging (GCD), Electrochemical Impedance Spectroscopy (EIS) and cyclic stability.

iii. Investigation of the composition and morphology-dependent chemical and physical properties of the synthesized nanocomposites by scanning electron microscopy (SEM), and X-ray diffraction (XRD).

iv. Rationalizing the electrochemical performance of synthesized Mn_xO_y, ZIF-67, ZIF-67-rGO, rGO-Mn_xO_y, and ZIF-67-rGO-Mn_xO_y with each other.

1.3 Energy storage devices

Producing the cleanest and most secure electrical energy is not only a problem to be resolved in the present period. Rather, storing the created power and using it for essential purposes in an effective manner are also seen as significant obstacles. Batteries are originally introduced in the middle of the 18th century for this function. Since then, developments in electrical energy storage systems have exploded, and in the 21st century, Lithium-ion battery advancements have achieved their pinnacle [14]. Lithium-ion batteries and other traditional energy storage devices such as Nickel-Cadmium batteries, Nickel Metal Hydride batteries, Lead-acid batteries, etc. power the majority of portable gadgets in use today. In addition to batteries, capacitors are another form of electrical energy storage device. The fundamental mechanisms of batteries and capacitors are quite similar [15]. It is essential to grasp the fundamental operational distinctions between capacitors and rechargeable (secondary) batteries. A battery typically consists of a positive electrode (cathode), a negative electrode (anode), and an electrolyte that permits ions to

travel from the anode to the cathode during discharge and back during recharging [16]. The voltage between the terminals of a battery varies based on the kind of battery and the chemistry between the electrodes and electrolytes. Electrochemical processes characteristic of rechargeable batteries and their operating voltages are shown in Figure 1.2 (a). The key distinction between batteries and capacitors is that batteries store energy in the bulk of chemical reactants capable of creating a charge, whereas capacitors store energy directly as surface charge. The reaction kinetics and mass transfer restrict battery discharge rates and hence power output, but similar constraints do not apply to capacitors, allowing for extraordinarily high power capability during both discharge and charge [17].

(a) **(b)** **(c)** **(d)**

Figure 1.1. Conventional (a) Lithium-ion (b) Nickel-cadmium (c) Lead-acid and (d) Nickel metal hydrate batteries.

Batteries have a high energy density but a low power density, while capacitors have a high power density but a low energy density. Energy and power are often used to describe the qualities of energy storage devices. Power density is defined as the quantity of electrical charge discharged by a device at one moment, while energy density is the ability of a device to store electrical charges. If the energy storage device is used in an electric car, for instance, the power density indicates how quickly one can go, while the energy density indicates how far one can travel on a single charge. Similar to the behavior of the water cup in Figure 1.2, capacitors produce huge power but store only minuscule quantities of energy (b). Comparable to the huge water bottle in Figure 1.2, batteries hold a considerable amount of charge but charge and discharge slowly (b). Although the energy density of batteries is sufficient, their power density is inadequate for powering heavy equipment such as electric automobiles, electric trains, and grid-level storage systems. To address the difficulties of electrical transformation and assure the use

of electricity in electric cars or grid-level storage, a new class of energy storage devices with optimal power and energy density is needed.

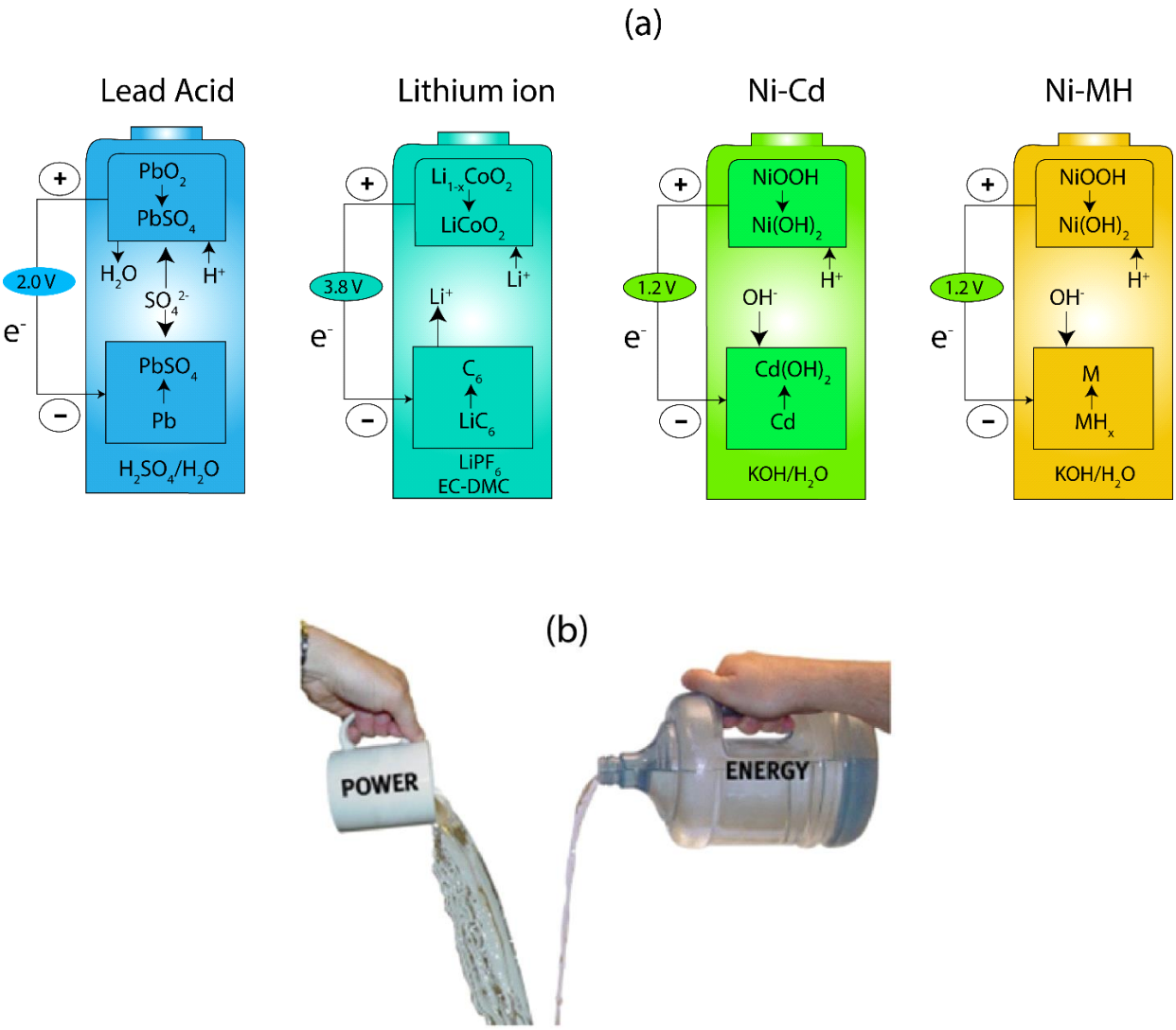

Figure 1.2. (a) Electrochemical behavior of several types of batteries. (b) Conceptualization of energy and power density. [18]

The supercapacitor or ultracapacitor is a revolutionary device that bridges the gap between capacitors and batteries. These energy storage devices possess key attributes that make them efficient and capable of combining the energy storage capabilities of batteries with the power discharge properties of traditional capacitors [19]. In the current market, there are three types of capacitors: electrostatic, electrolytic, and electrochemical or supercapacitors [20]. Because

electrostatic capacitors retain electrical charge via physical processes, they have the lowest energy density of the three kinds. Electrolytic capacitors function by increasing insolation on a rough metal surface, such as etched aluminum, and this form of capacitor has a tenfold greater energy density than electrostatic capacitors [21].

However, electrochemical capacitors use electric double-layer capacitance (EDLC) at the solid electrolyte interface, resulting in a capacitance that is 10,000 times larger than electrolytic capacitors [22]. The capacitor stores charge electrostatically in an electric field, and its capacitance, C, is a function of the area of the metal plates, A, and the distance between them, d. Typical capacitors have d 1 m and A m^2 (see Figure 1.4). To enhance the amount of charge held, it is necessary to reduce d and maximize A, and a supercapacitor does this. A supercapacitor has two electrodes separated by an ion-permeable separator to avoid short circuits, and a cell impregnated with a liquid electrolyte [23]. As a supercapacitor's potential is applied, ions from the electrolyte seep into the pores of the electrode with the opposite charge. At the interface of the electrodes and the electrolyte, charge accumulates to produce two charged layers (known as electric double layers) with a separation distance on the order of 1 nm. Activated carbon is used as the active electrode material in contemporary supercapacitor technology because it is electrically conductive and has an exceptionally large surface area on the order of 1000-2000 m^2/g, allowing high capacitance values to be attained in a compact volume. Comparing a capacitor with a supercapacitor of comparable volume as seen in Figure: 1.3, the capacitor stores just 0.003 F, whereas the supercapacitor stores >10,000 times more charge - around 50 F.

- Numerous benefits of supercapacitors over traditional energy storage devices make their use in the future generation of cars viable.
- The performance of supercapacitors falls between that of regular capacitors and batteries. They provide more energy density than standard capacitors and greater power density than batteries.
- Supercapacitors can be charged in seconds, while batteries and capacitors need hours and milliseconds, respectively.

- Supercapacitors store charges in a very reversible manner. Typical rechargeable batteries only survive a few hundred charge/discharge cycles, but supercapacitors may be used up to one million times.
- As opposed to traditional batteries, there are no heavy metals or disposal difficulties with these batteries.
- Supercapacitors are capable of operating under harsh circumstances. Supercapacitors, for instance, may be utilized at temperatures as low as 40 °C, but batteries cannot work at such low temperatures.
- Maintenance-free—offering greater cost-over-life and fit-and-forget functionality.

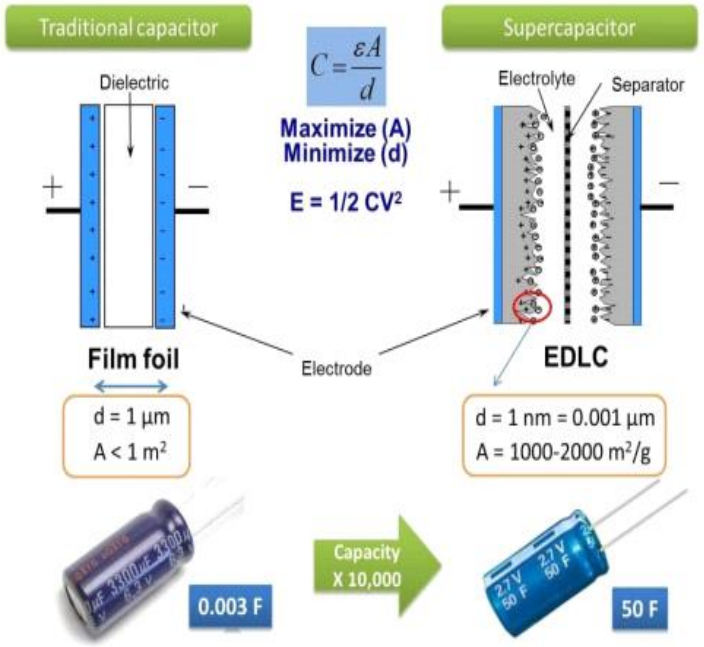

Figure: 1.3. Comparison between conventional capacitor and supercapacitor. [24]

Based on their manner of storage, electrochemical capacitors may be loosely divided into two categories: double-layer capacitors and pseudocapacitors. EDLC stores electrical energy without charge transfer at the phase boundary between an electrode (electronic conductor) and the electrolyte solution (liquid ionic conductor). In addition, the current generated by this kind of capacitor is mostly a displacement current resulting from charge rearrangement, also known as a completely polarized electrode.

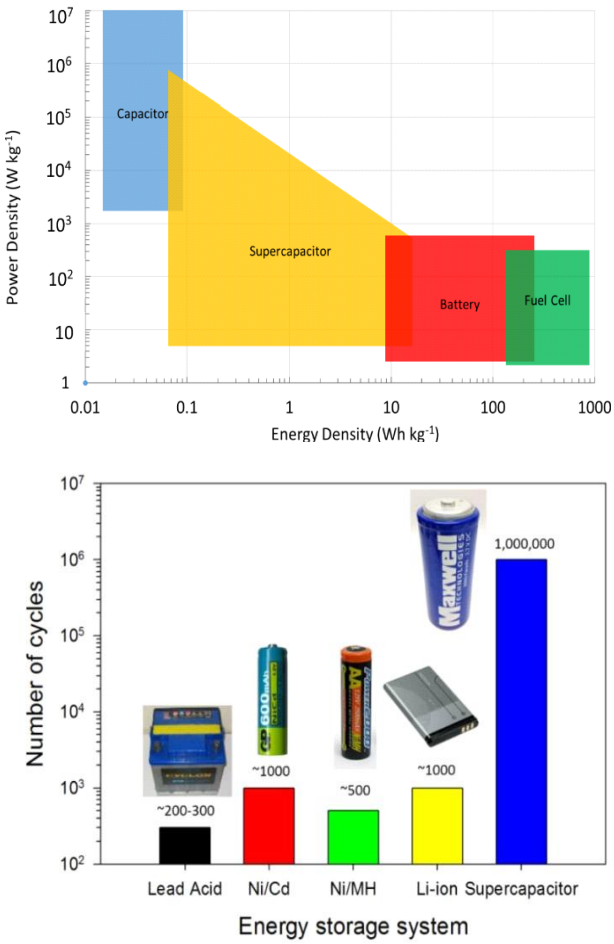

Figure: 1.4. (a) Comparison of energy and power density of energy storage devices, and (b) Cyclic stability of storage devices.

The creation of a layer on the electrodes is known as the Helmholtz layer. In contrast, rapid faradaic redox processes generated by redox-active species involving metal oxides and conducting polymers with electrolytes drive the charge storage mechanism of pseudocapacitors [25]. In comparison to EDLC-based materials, the capacitance and power density of pseudocapacitors are adequate; yet, their cyclic stability is so low that pseudocapacitors alone cannot satisfy the commercially critical criterion for cyclic stability. The unstable cyclic stability is caused by damaging redox reactions because, during these reactions, the surface morphology changes its phases and restricts accessible surfaces for incoming electrolytes. To do this, hybrid capacitors are added to the supercapacitors family by fusing these two kinds (EDLC and pseudocapacitors). As it stores charges in both faradic and non-faradic modes, this novel hybrid

form of capacitors will ultimately be able to simultaneously meet energy and power density requirements. Therefore, supercapacitors have a wide variety of applications not only in electronics but also in cars. These devices are built with a range of capacitance levels to meet a variety of industry specifications. Supercapacitors ranging from 1 F to 150 F are used in electronic devices including mobile phones, digital cameras, medical equipment, and uninterruptible power sources. In the meanwhile, supercapacitors with a capacitance range of 300 F to 350 F are required for power backup in industrial and telecom-based stations and renewable energy systems. Supercapacitors with a higher capacitance (650 F to 3000 F) are suited for automotive subsystems, hybrid drive trains, rail system power, heavy transportation, and other applications. In addition, this technology has resolved environmental concerns by making it possible to regulate the disposal of used batteries, which may result in significant waste. In addition, market interest in supercapacitors is anticipated to increase as a result of their increased power and longer shelf life, which may result in a greener environment.

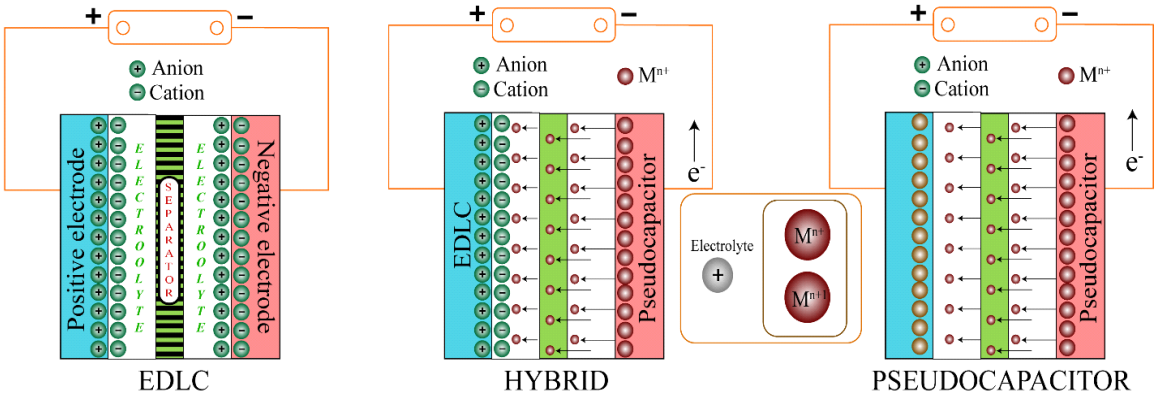

Figure 1.5. Charge storing mechanism of (a) EDLC (b) Hybrid and (c) Pesudocapacitor supercapacitor. [26]

The creation of a layer on the electrodes is known as the Helmholtz layer. In contrast, rapid faradaic redox processes generated by redox-active species involving metal oxides and conducting polymers with electrolytes drive the charge storage mechanism of pseudocapacitors [26]. In comparison to EDLC-based materials, the capacitance and power density of pseudocapacitors are adequate; yet, their cyclic stability is so low that pseudocapacitors alone cannot satisfy the commercially critical criterion for cyclic stability. The unstable cyclic stability is caused by damaging redox reactions because, during these reactions, the surface morphology

changes its phases and restricts accessible surfaces for incoming electrolytes. To do this, hybrid capacitors are added to the supercapacitors family by fusing these two kinds (EDLC and pseudocapacitors). As it stores charges in both faradic and non-faradic modes, this novel hybrid form of capacitors will ultimately be able to simultaneously meet energy and power density requirements.

Therefore, supercapacitors have a wide variety of applications not only in electronics but also in cars. These devices are built with a range of capacitance levels to meet a variety of industry specifications. Supercapacitors ranging from 1 F to 150 F are used in electronic devices including mobile phones, digital cameras, medical equipment, and uninterruptible power sources.[27] In the meanwhile, supercapacitors with a capacitance range of 300 F to 350 F are required for power backup in industrial and telecom-based stations and renewable energy systems. Supercapacitors with a higher capacitance (650 F to 3000 F) are suited for automotive subsystems, hybrid drive trains, rail system power, heavy transportation, and other applications.[28] In addition, this technology has resolved environmental concerns by making it possible to regulate the disposal of used batteries, which may result in significant waste. In addition, market interest in supercapacitors is anticipated to increase as a result of their increased power and longer shelf life, which may result in a greener environment.

1.4 ZIF AND ZIF-67-based supercapacitor materials

Metal-organic frameworks (MOFs), also known as coordination polymers, have piqued the curiosity of the material and chemistry communities during the last decade. Metal centers (clusters/ions) are joined together by organic linkers (usually consisting of imidazolate/carboxylate or groups) to produce crystalline, elongated, and frequently highly porous structures in MOFs. MOFs have several benefits over traditional porous materials, including the ability to rationally design the building of the most desired crystal structures and perform crystal engineering.[29] Furthermore, extreme synthetic flexibility and simplicity of incorporating multiple chemical functions; customizing lightweight organic linkers that give ultrahigh surface area and remarkable porosity previously unavailable to traditional materials (such as zeolites and porous carbon).[30] As a result of their adjustable and intriguing shape, high specific surface area, many pores, and multi-functionalities, metal-organic frameworks (MOFs) are in the hottest research period. Supercapacitors have a low energy density despite

their high power density. As a result, MOFs may be fine-tuned for specific applications, such as selecting certain metal positions and changing pore widths to balance power and energy densities. As a consequence, elucidating the unique process underlying MOFs; extraordinary shape, functional linkers, particular surface area, and presence of metal sites, as well as their related electrochemical performance, is critical. A MOF class, Zeolitic imidazolate frame (ZIFs), may be manufactured by mixing organic and inorganic ingredients having diverse features such as distinct particle morphologies, extraordinary porosities, and surface functionality. ZIFs are being investigated as a template for the fabrication of porous carbon/metal oxides, among other things, due to their porous structure.[31] The enhanced pores of the surface area can be exploited for interfacial transport as well as providing smaller diffusion channels for the electrolyte. The advantages of ZIF-derived carbons include ease of preparation and intrinsic variety, as well as precise control of physicochemical characteristics. Zeolitic imidazolate framework-67 (ZIF-67), and ZIF-8 are all MOFs, but ZIF-67 (2-methyl imidazolate as a linker and cobalt as a metal supply) stands out for its better electronic conductivity and ease of preparation.[32] When ZIF-67 nanostructures are doped with metals/ their oxides viz. Ru, Ni, ZnO, NiO, and MnxOy, the properties like surface area, porosity, chemical, and thermal stability of modified ZIF-67 are improved compared with the pure form.

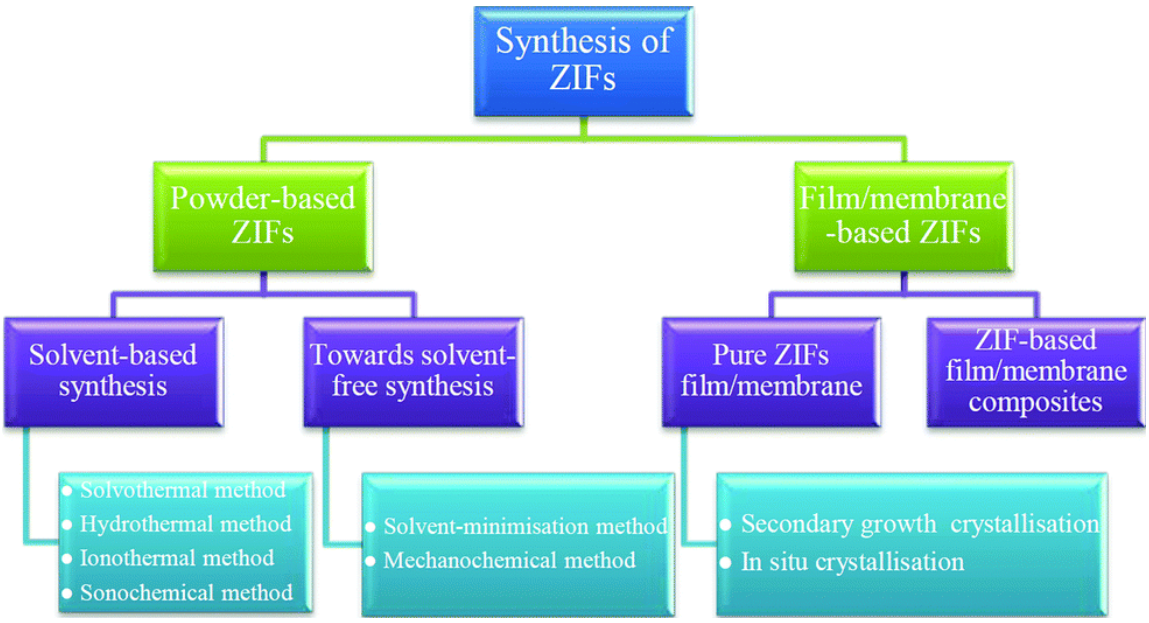

Figure 1.6. Summary of different synthesis methods for ZIF-based materials.

Table 1.1. Previous works of ZIF-67 and composite of ZIF-67 as energy storage devices.

No	Electrode material	Electrolyte	Scan rate/current density	Specific Capacitance (Fg^{-1})	Capacity retention %	Ref
1	ZIF-67/PANI1	3 M KCl	10 mV s^{-1}	371	80	33
2	ZIF-67/polypyrrole nanotubes	1 M Na_2SO_4	0.5 Ag^{-1}	597.6	90.7	34
3	ZIF67/rGO composite	0.2 M $K_3[Fe(CN)_6]$+1M Na_2SO_4	4.5 Ag^{-1}	1453	90.5 1000cycles	35
4	ZIF67/Co_3O_4@C	1 M LiOH	1 Ag^{-1}	251	90 5000 cycle	36
5	ZIF-67/Co_3O_4	2 M KOH	5 Ag^{-1}	190	72.45 5000 cycle	37
6	ZIF-67/C	0.5m H_2SO_4	20 mVs^{-1}	238	72 200	38
7	ZIF67/C@CNT	6 M KOH	10 mVs^{-1}	343	13 1000	39

1.5 Effect of TMOs in high-performing SC

TMOs with accessible changeable oxidation states are notable prospects for pseudocapacitor materials [40]. Different TMOs, including Ruthenium oxide (RuO_2), have been researched extensively for their capacitance performance [41]. However, the material's lack of natural availability, high price, the complexity of production procedures, and toxicity have restricted its practical energy storage uses. Due to their cheap cost, availability, and environmental friendliness, manganese oxide-based pseudo-capacitive materials are a preferable option to other TMOs [42]. However, the predicted (1370 Fg^{-1}) and observed specific capacitance of MnO_2-based materials [43] vary significantly. The principal limitations of manganese-based compounds are their electrochemical dissolution and low electrical conductivity. Therefore, the key to designing high-performance hybrid supercapacitor materials is to increase the accessibility of electrolytes and electron transport via the right nano-architecture and

morphology. However, this issue may be handled by using composites of mixed or binary transition metal oxides created with carbonaceous materials such as rGO, which might boost the charge transfer rate in addition to the rapid redox reaction [44]. It is anticipated that the synergistic impact of mixed metal oxides or hydroxides with rGO would ease the transfer of electrical charge inside the electrode, hence considerably enhancing its performance. The increased and curved surface area of rGO has a significant effect on the capacitance of mixed metal oxides and hydroxides. Because integration always makes it easier for the expanding rGO layers to insert/eject electrolyte ions from the electrodes. Due to the high aggregation of rGO sheets, the manufacture of numerous oxides or hydroxides of transitional metals inside rGO layers is often exceedingly difficult. In addition, the electrical conductivity and well-defined shape of metal oxides or hydroxides depend totally on the synthesis procedure. In such instances, manganese oxides may be changed with other metal oxides or hydroxides, such as Ni, Co, etc.

Table 1.2: Previous works of manganese oxides and rGO-based materials as energy storage devices.

No	Materials	Electrolyte	Specific capacitance (Fg^{-1})	Rate capability/F g^{-1}	Stability (Cycle)	Ref
1	MWCNT/MnO_2	1 M Na_2SO_4	603.88 (10 mV s^{-1})	405.15 (100mVs^{-1})	81% (1,000)	45
2	MnO_2/GO	1 M Na_2SO_4	360.3 (0.5 A g^{-1})	223.6 (5 A g^{-1})	>93% (1,000)	46
3	MnO_2/rGO	1 M Na_2SO_4	234.8 (0.1 A g^{-1})	136.9 (5 A g^{-1})	100% (10,000)	47
4	MnO_2/graphene	1 M Na_2SO_4	133 (10 mV s^{-1})	104 (150mVs^{-1})	75% (10,000)	48
5	MnO_2/graphene	1 M KOH	342.8 (0.5 A g^{-1})	111.2 (20 A g^{-1})	90.3% (3,000)	49
6	Graphene/MnO_2/CNTs	1 M Na_2SO_4	372 (0.5 A g^{-1})	194 (10 A g^{-1})	>90% (3,000)	50
7	N-doped graphene/MnO_2	1 M Na_2SO_4	411.5 (0.5 A g^{-1})	242 (20Ag^{-1})	88.3% (4,000)	51
8	Sponge@rGO@MnO_2	1 M Na_2SO_4	205 (0.1 A g^{-1})	136.9 (5 A g^{-1})	90% (20,000)	52

References

1. Usai, L., Lamb, J. J., Hertwich, E., Burheim, O. S., & Strømman, A. H. (2022). Analysis of the Li-ion battery industry in light of the global transition to electric passenger light duty vehicles until 2050. Environmental Research: Infrastructure and Sustainability, 2(1), 011002.
2. Yang, J., Gu, F., & Guo, J. (2020). Environmental feasibility of secondary use of electric vehicle lithium-ion batteries in communication base stations. Resources, Conservation and Recycling, 156, 104713.
3. Olabi, A. G., Abbas, Q., Al Makky, A., & Abdelkareem, M. A. (2022). Supercapacitors as next generation energy storage devices: Properties and applications. Energy, 248, 123617.
4. Najib, S., & Erdem, E. (2019). Current progress achieved in novel materials for supercapacitor electrodes: mini review. Nanoscale Advances, 1(8), 2817-2827.
5. Liu, Y., Jiang, S. P., & Shao, Z. (2020). Intercalation pseudocapacitance in electrochemical energy storage: recent advances in fundamental understanding and materials development. Materials Today Advances, 7, 100072.
6. Ke, Q., & Wang, J. (2016). Graphene-based materials for supercapacitor electrodes–A review. Journal of Materiomics, 2(1), 37-54.
7. Singh, K. P., Bhattacharjya, D., Razmjooei, F., & Yu, J. S. (2016). Effect of pristine graphene incorporation on charge storage mechanism of three-dimensional graphene oxide: superior energy and power density retention. Scientific reports, 6(1), 1-10.
8. Shan, Y., Zhang, M., Bai, Y., Du, M., Guo, X., & Pang, H. (2022). Design and synthesis of transition metal oxide/zeolitic imidazolate framework-67 composites. Chemical Engineering Journal, 429, 132146.
9. Sundriyal, S., Shrivastav, V., Kaur, H., Mishra, S., & Deep, A. (2018). High-performance symmetrical supercapacitor with a combination of a ZIF-67/rGO composite electrode and a redox additive electrolyte. ACS omega, 3(12), 17348-17358.
10. Sundriyal, S., Shrivastav, V., Mishra, S., & Deep, A. (2020). Enhanced electrochemical performance of nickel intercalated ZIF-67/rGO composite electrode for solid-state supercapacitors. International Journal of Hydrogen Energy, 45(55), 30859-30869.

11. Yuan, C., Su, L., Gao, B., & Zhang, X. (2008). Enhanced electrochemical stability and charge storage of MnO2/carbon nanotubes composite modified by polyaniline coating layer in acidic electrolytes. Electrochimica Acta, 53(24), 7039-7047.
12. Zhang, S. W., & Chen, G. Z. (2008). Manganese oxide based materials for supercapacitors. Energy Materials, 3(3), 186-200.
13. Béguin, F., Presser, V., Balducci, A., & Frackowiak, E. (2014). Carbons and electrolytes for advanced supercapacitors. Advanced materials, 26(14), 2219-2251.
14. Sridhar, S., & Salkuti, S. R. (2022). Development and Future Scope of Renewable Energy and Energy Storage Systems. Smart Cities, 5(2), 668-699.
15. Abruña, H. D., Kiya, Y., & Henderson, J. C. (2008). Batteries and electrochemical capacitors. Phys. Today, 61(12), 43-47.
16. Wang, X., Lu, X., Liu, B., Chen, D., Tong, Y., & Shen, G. (2014). Flexible energy-storage devices: design consideration and recent progress. Advanced materials, 26(28), 4763-4782.
17. Weber, A. Z., Mench, M. M., Meyers, J. P., Ross, P. N., Gostick, J. T., & Liu, Q. (2011). Redox flow batteries: a review. Journal of applied electrochemistry, 41(10), 1137-1164.
18. Gao, C., Huang, J., Xiao, Y., Zhang, G., Dai, C., Li, Z., ... & Qu, L. (2021). A seamlessly integrated device of micro-supercapacitor and wireless charging with ultrahigh energy density and capacitance. Nature communications, 12(1), 1-10.
19. Kebede, A. A., Kalogiannis, T., Van Mierlo, J., & Berecibar, M. (2022). A comprehensive review of stationary energy storage devices for large scale renewable energy sources grid integration. Renewable and Sustainable Energy Reviews, 159, 112213.
20. Jayalakshmi, M., & Balasubramanian, K. (2008). Simple capacitors to supercapacitors-an overview. Int. J. Electrochem. Sci, 3(11), 1196-1217.
21. Braham, A., Lahyani, A., Venet, P., & Rejeb, N. (2009). Recent developments in fault detection and power loss estimation of electrolytic capacitors. IEEE Transactions on Power Electronics, 25(1), 33-43.
22. Shukla, A. K., Sampath, S., & Vijayamohanan, K. (2000). Electrochemical supercapacitors: Energy storage beyond batteries. Current science, 79(12), 1656-1661.

23. Gidwani, M., Bhagwani, A., & Rohra, N. (2014). Supercapacitors: the near future of batteries. International Journal of Engineering Inventions, 4(5), 22-27.
24. Ehsani, A., Kowsari, E., Najafi, M. D., Safari, R., & Shiri, H. M. (2017). Influence of ionic liquid on pseudocapacitance performance of electrochemically synthesized conductive polymer: Electrochemical and theoretical investigation. Journal of colloid and interface science, 500, 315-320.
25. Chen, K., Yang, Y., Li, K., Ma, Z., Zhou, Y., & Xue, D. (2014). CoCl2 designed as excellent pseudocapacitor electrode materials. ACS Sustainable Chemistry & Engineering, 2(3), 440-444.
26. Chodankar, N. R., Pham, H. D., Nanjundan, A. K., Fernando, J. F., Jayaramulu, K., Golberg, D., ... & Dubal, D. P. (2020). True meaning of pseudocapacitors and their performance metrics: asymmetric versus hybrid supercapacitors. Small, 16(37), 2002806.
27. Lasrado, D., Ahankari, S., & Kar, K. K. (2021). Global Trends in Supercapacitors. In Handbook of Nanocomposite Supercapacitor Materials III (pp. 329-365). Springer, Cham.
28. Burke, A. (2010). Ultracapacitor technologies and application in hybrid and electric vehicles. International Journal of Energy Research, 34(2), 133-151.
29. Wang, C., Liu, D., & Lin, W. (2013). Metal–organic frameworks as a tunable platform for designing functional molecular materials. Journal of the American Chemical Society, 135(36), 13222-13234.
30. Cao, S., Li, B., Zhu, R., & Pang, H. (2019). Design and synthesis of covalent organic frameworks towards energy and environment fields. Chemical Engineering Journal, 355, 602-623.
31. Zhong, G., Liu, D., & Zhang, J. (2018). The application of ZIF-67 and its derivatives: adsorption, separation, electrochemistry and catalysts. Journal of Materials Chemistry A, 6(5), 1887-1899.
32. Vu, M. T. (2019). Mixed matrix membranes for gas separation.
33. Zhang, F.; Hao, L.; Zhang, L.; Zhang, X. Solid-state thermolysispreparation of Co3O4nano/micro superstructures from metal-organicframework for supercapacitors. Int. J. Electrochem. Sci. 2011,6, 2943− 2954

34. Xu, X.; Tang, J.; Qian, H.; Hou, S.; Bando, Y.; Hossain, M. S.A.; Pan, L.; Yamauchi, Y. Three-Dimensional Networked Metal-Organic Frameworks with Conductive Polypyrrole Tubes for FlexibleSupercapacitors. ACS Appl. Mater. Interfaces 2017,9, 38737−38744.
35. Sundriyal, S., Shrivastav, V., Kaur, H., Mishra, S., & Deep, A. (2018). High-performance symmetrical supercapacitor with a combination of a ZIF-67/rGO composite electrode and a redox additive electrolyte. ACS omega, 3(12), 17348-17358.
36. Lee, D.; Yoon, S.; Shrestha, N.; Lee, S.; Ahn, H.; Han, S. Unusual energy storage and charge retention in Co-based metal–organic frameworks. Micropor. Mesopor. Mat. 2012, 153, 163–165
37. Saraf, M.; Rajak, R.; Mobin, S. MOF derived high surface area enabled porous Co3O4 nanoparticles for supercapacitors. ChemistrySelect 2019, 4, 8142–8149.
38. Torad, N.; Salunkhe, R.; Li, Y.; Hamoudi, H.; Imura, M.; Sakka, Y.; Yamauchi, Y. Electric double-layer capacitors based on highly graphitized nanoporous carbons derived from ZIF-67. Chem.-Eur. J. 2014, 20, 7895–7900.
39. Gao, T.; Zhou, F.; Ma, W.; Li, H. Metal-organic-framework derived carbon polyhedron and carbon nanotube hybrids as electrode for electrochemical supercapacitor and capacitive deionization. Electrochim. Acta 2018, 263, 85–93
40. Moysiadou, A., & Hu, X. (2019). Stability profiles of transition metal oxides in the oxygen evolution reaction in alkaline medium. Journal of Materials Chemistry A, 7(45), 25865-25877.
41. Liang, R., Du, Y., Xiao, P., Cheng, J., Yuan, S., Chen, Y., ... & Chen, J. (2021). Transition metal oxide electrode materials for supercapacitors: a review of recent developments. Nanomaterials, 11(5), 1248.
42. Zhang, S. W., & Chen, G. Z. (2008). Manganese oxide based materials for supercapacitors. Energy Materials, 3(3), 186-200.
43. Qian, Y., Lu, S., & Gao, F. (2011). Preparation of MnO2/graphene composite as electrode material for supercapacitors. Journal of Materials Science, 46(10), 3517-3522.
44. Zhang, H., Gao, Q., Li, Z., Xu, P., Xiao, H., Zhang, T., & Liang, X. (2020). A rGO-Based Fe2O3 and Mn3O4 binary crystals nanocomposite additive for high performance Li–S battery. Electrochimica Acta, 343, 136079.

45. Li, W. S., Chang, M. L., Chuang, K. C., Li, Y. S., Luo, J. D., & Cheng, H. C. (2019). Electrochemical properties of CNT/MnO2 hybrid nanostructure with low-temperature hydrothermal synthesis as high-performance supercapacitor. Journal of the Electrochemical Society, 166(10), A2194.
46. Dai, K., Lu, L., Liang, C., Dai, J., Liu, Q., Zhang, Y., ... & Liu, Z. (2014). In situ assembly of MnO2 nanowires/graphene oxide nanosheets composite with high specific capacitance. Electrochimica Acta, 116, 111-117.
47. Chen, Y., Zhang, J., Li, M., Yang, C., Zhang, L., Wang, C., & Lu, H. (2018). Strong interface coupling and few-crystalline MnO2/Reduced graphene oxide composites for supercapacitors with high cycle stability. Electrochimica Acta, 292, 115-124.
48. Amade, R., Muyshegyan-Avetisyan, A., Martí González, J., Pérez del Pino, A., György, E., Pascual, E., ... & Bertran Serra, E. (2019). Super-capacitive performance of manganese dioxide/graphene nano-walls electrodes deposited on stainless steel current collectors. Materials, 12(3), 483.
49. Wang, H., Fu, Q., & Pan, C. (2019). Green mass synthesis of graphene oxide and its MnO2 composite for high performance supercapacitor. Electrochimica Acta, 312, 11-21.
50. HB, C. Y. L. S. Z. (2012). Varanasi CV Liu J Synergistic effects from graphene and carbon nanotubes enable flexible and robust electrodes for high-performance supercapacitors. Nano Lett, 12(8), 4206-4211.
51. Le, Q. J., Huang, M., Wang, T., Liu, X. Y., Sun, L., Guo, X. L., ... & Zhang, Y. X. (2019). Biotemplate derived three dimensional nitrogen doped graphene@ MnO2 as bifunctional material for supercapacitor and oxygen reduction reaction catalyst. Journal of colloid and interface science, 544, 155-163.
52. Jin, G. E., Honghin, Y. A. O., & Wei, H. U. (2013). Facile dip coating processed graphene/MnO2 nanostmctured sponges as high performance supercapaeitor electrodes. Nano Energy, 2(4), 505-513.

CHAPTER 2
EXPERIMENTAL SECTION

2.1 Materials and Chemicals

In this study, analytical grade Graphite flakes (99%, Alfa Aesar), Conc. H_2SO_4 (98%, Merck), $KMnO_4$ (>99%, Sigma Aldrich), dilute HCl (37%, Merck), H_2O_2 (30% Merck), Cobalt(II) nitrate hexahydrate (>99%, Sigma Aldrich), 2-Methylimidazole (>99%, Sigma Aldrich), Glycerol (JHD, China) and Ethanol (Merck, Germany) were purchased and used without further purification. Aqueous solutions for all the experiments were prepared using deionized (DI) water (18.2 MΩ-cm of resistivity at 25 ℃).

2.2 Synthesis of Mn_xO_y

To produce manganese oxide, a simple gel-forming method was applied. [1] This technique began with the preparation of 0.3 M 100 mL $KMnO_4$ in a beaker. Then, a 0.3 M, 50 mL solution of glycerol was prepared. The Glycerol solution was then filled into a burette and introduced drop by drop to the $KMnO_4$ solution while continuous magnetic stirring was done.

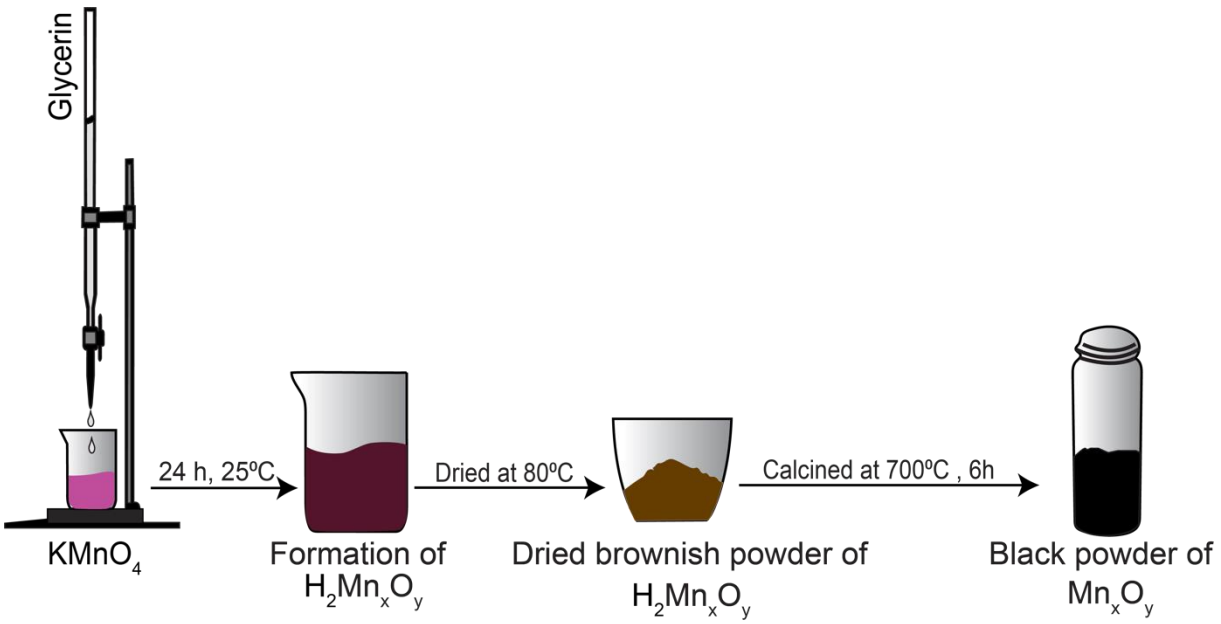

Figure 2.1. Schematic diagram of Mn_xO_y preparation by gel formation method.

After merging the whole glycerol solution, a gel-like solution with a brown hue was seen. For the next thirty minutes, the event was permitted to continue. The gel was left alone for the next twenty-four hours.

After 24 hours, the gel in the beaker had settled. The supernatant was separated so that the gel could be properly dried at 80°C on a hotplate. Then, it was collected and preserved in a mortar and pestle. The powder was pulverized and washed with distilled water. The material was then stirred many times to remove any residual K^+ ions. After being washed with water, the gel was again rinsed with alcohol to eliminate any traces of glycerol. The products were dried in an 80°C hot air oven for 12 hours after washing. A brownish powder was collected and a part of the recovered material was placed in a vial, while the rest was calcined at 700°C for six hours to produce black manganese oxide (Mn_xO_y).

2.3 Synthesis of GO

A two-step chemical oxidation technique was applied to make the GO used in this study [2-5]. H_2SO_4 and HNO_3 (in a 3:1 ratio) were mixed in a 500 mL glass beaker and continuously magnetically agitated in an oil bath at 80°C.

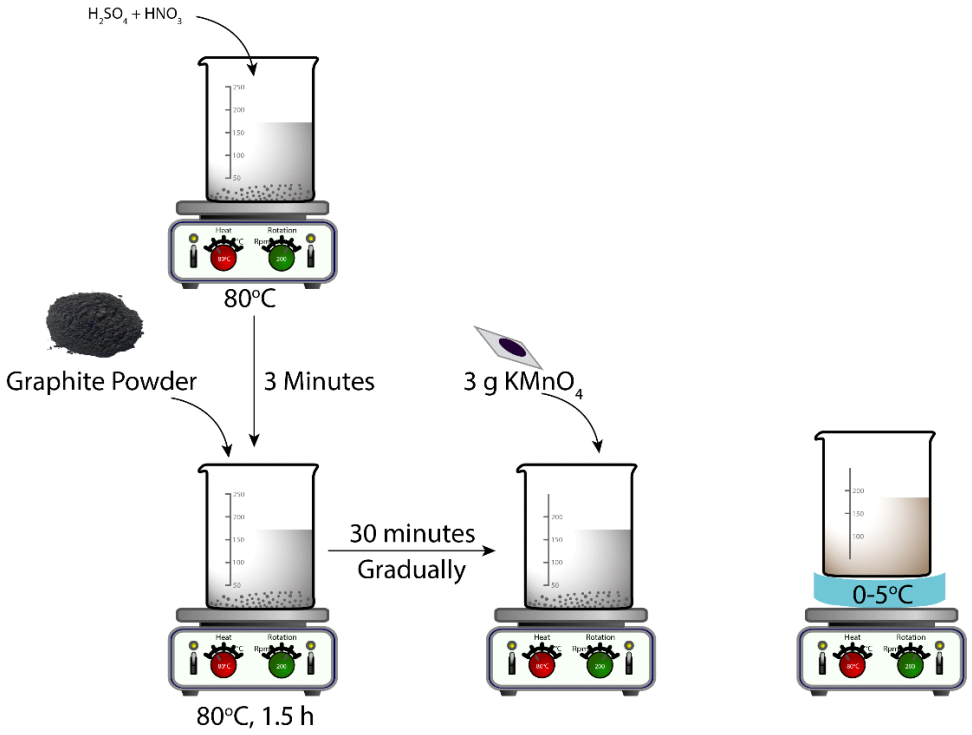

Figure 2.2. Schematic diagram of GO synthesis

After 3 minutes, 0.5 g of graphite flakes (1 wt %) were added to the flask, which was kept at 80°C for 1.5 hours with steady stirring. This method is used to do early graphite oxidation. The beaker was gradually filled with 3 g of $KMnO_4$ (2%) over the course of 30 minutes before being put in an ice bath (0–5)°C. After filling the beaker with the thick brown paste, it was placed in an oil bath at 45°C and vigorously stirred for 1 hour, until it developed a thick brown paste.

The temperature was then raised to 90°C, and 50 mL of DI water was slowly added to the solution while constantly stirring for 15 minutes. Following that, the oil bath was removed, and 50 mL of H_2O_2 was added to the mixture to reduce the amount of $KMnO_4$ in the solution. A vivid yellow solution appeared afterward. The solution was washed and filtered many times with aqueous HCl solution (37 percent HCl: DI water = 10:100 ml), and it was then dialyzed in water to obtain neutral pH values in an aqueous environment until the neutral pH has obtained. For 10 minutes, the solution was centrifuged at 4000 rpm in a centrifuge machine. The GO was produced by drying the filtrate formed after this procedure in a vacuum oven at 40°C for 24 hours.

2.4 Conversion of GO into rGO

A simple hydrothermal reaction was adopted to convert the as-prepared GO to rGO.[6] In brief, 0.2 g of as-prepared GO was sonicated for 2 hours in a combination of 50 mL DI water and 10 mL of glycerin. The GO suspension was then placed in a stainless-steel autoclave and heated for 24 hours at 180°C to generate a gel-like product. Afterward, the product was washed repeatedly with DI water and dried for 6 hours at 80°C.

2.5 Synthesis of ZIF-67

Pure aqueous solutions can be used to make ZIF-67 (zeolitic imidazolate framework- 67) nanocrystals at room temperature.[7] To begin, deionized (DI) water was used to dissolve cobalt nitrate hexahydrate ($Co(NO_3)_2$) and 2-methylimidazole (Hmim). At room temperature, these two solutions were combined and stirred for 24 hours. The precipitates were then centrifuged before being rinsed with water and methanol. Finally, vacuum-dried and the ZIF-67 nanomaterial were obtained. This procedure not only decreases or eliminates the usage of harmful organic solvents but also minimizes the cost of manufacturing ZIF-67, which fully overcomes the above issues.

2.6 Synthesis of ZIF-67-rGO

0.3g of GO was initially sonicated with water for two hours to ensure appropriate dispersion. After then, 5.5g of 2-methylimidazol was added as a linker along with 0.45g of $Co(NO_3)_2$. $6H_2O$ and 3ml of water. The beaker was then transported to the autoclave at 180°C for 24 hours while being continuously stirred. A purple gel-like substance was found. The product was cleaned in DI water and alcohol, then dried overnight at 80°C. ZIf-67-rGO, the requested item, was discovered. [8-10]

2.7 Synthesis of rGO-Mn_xO_y

A one-step hydrothermal reduction method (180°C for 24 hours) was applied to produce the rGO-Mn_xO_y composite.[11] 0.5 mM $KMnO_4$ solution was prepared and slowly added into a combination of glycerol (5 mL) and 2.0 g of a homogenous aqueous suspension of GO (0.20 g, 1.44 wt%). The final vessel was then filled with H_2O (3.0 mL) and glycerol (10 mL). The suspension was transferred to a 100 mL Teflon autoclave, sealed, and held at 180°C for 24 hours. Following the hydrothermal reaction, a gel-like substance was discovered, which was washed and dried to yield the rGO-Mn_xO_y nanocomposite.

2.8 Preparation of ZIF-67-rGO-Mn_xO_y

To begin, GO was produced using a modified hammer approach. 0.3g of powdered GO was dispersed in 20 mL of water, then 0.45g of $Co(NO_3)_2$. $6H_2O$ was added to the GO solution with 3 mL of water and 5.5g of Hmim was added with continuous stirring for 30 minutes. Then, while stirring, 0.04 M of 10 mL $KMnO_4$ was added to the mixture, and it was held for 24 hours under vigorous stirring. The solution was then transferred to a Teflon autoclave with a capacity of 100 mL. After that, the autoclave was sealed and left at 180°C for 24 hours to allow the ZIF-67-rGO-Mn_xO_y hybrid material to develop. To obtain ZIF-67-rGO-Mn_xO_y nanocomposite, the product will be washed and dried.

2.9 Cell setup and electrochemical measurement

At 25°C in 0.5 M Na_2SO_4, the electrochemical characteristics of the as-prepared synthetic materials were studied in a two-electrode cell setup. The electrode materials were initially placed in a glass vial containing 250 µl of N-Methyl-2-pyrrolidone (NMP) solution as solvent and

PVDF (Polyvinylidene fluoride) as a binder. After that, the glass vial was sonicated for 30 minutes to get a slurry of active components. On two polished disk-shaped graphite electrodes, around 2 µl (2mgcm^{-2}) of the slurry was pasted. To evaporate all of the solvents, both electrodes were dried in a hot air oven at 60°C for 3-5 hours. After that, one of the electrodes was positioned into the split coin cell, and a separator made of Whatman Filter Paper (pore size, 11µm) was gently put on top of it. On the filter paper, a few drops of freshly made 0.5 M Na_2SO_4 were applied. When the filter paper appears to be wet, another electrode is placed upside down on top of it. Finally, the split coin cell's cap was properly assembled to finish the cell setup.

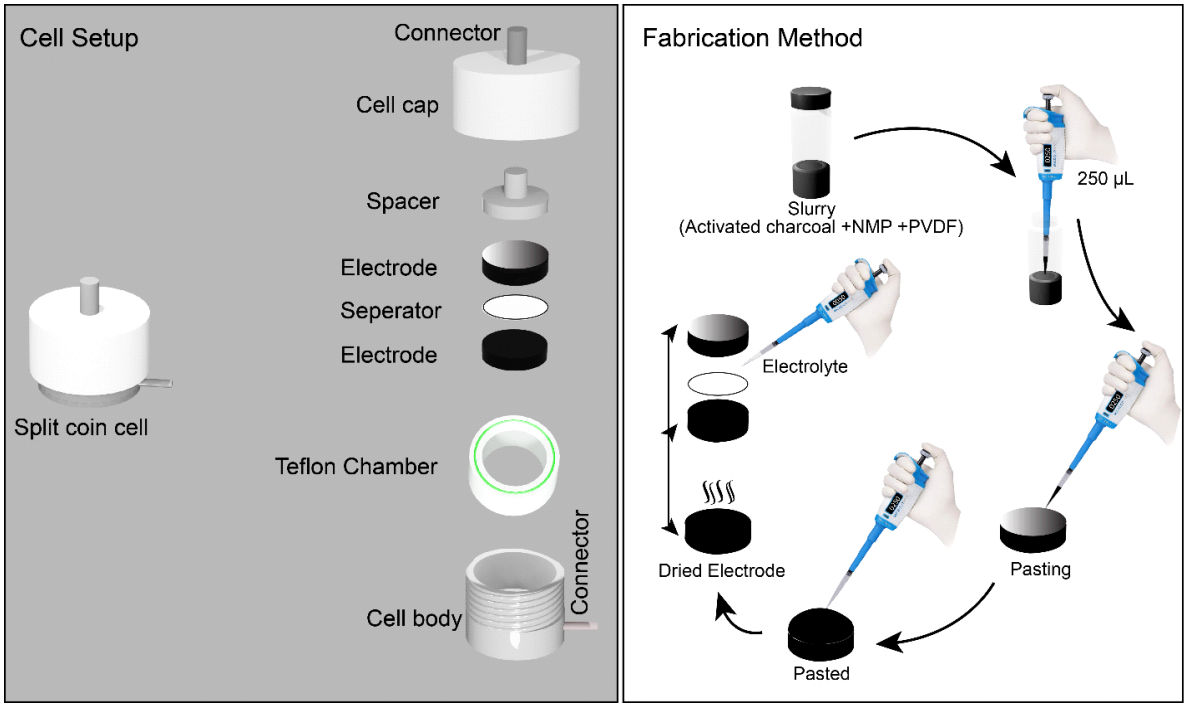

Figure 2.3: Symmetrical assemblies of two-electrode setup and electrochemical data acquisition.

Electrochemical investigations were accomplished with a computer-controlled electrochemical workstation (CHI 660E, USA) using a two-electrode system. The electrochemical properties of the fabricated supercapacitors were investigated using cyclic voltammetry (CV), galvanostatic charging discharging (GCD), and electrochemical impedance spectroscopy (EIS). The analyses were carried out in 0.5 M Na_2SO_4. CV analyses were carried out at different scan rates from 10 to 100 mV s^{-1}. Besides, the GCD was performed within this potential to find the specific capacitance, energy density, and power density. The EIS was performed within the frequency range from 0.01 Hz to 100 kHz at an AC amplitude of 10 mV at room temperature at the open

circuit potential. It was performed to observe the electrochemical series resistance value of the electrode setup with different electrolytes. Lastly, the cyclic stability tests were performed using 10000 consecutive cycles. The specific capacitance (C_{sp}), specific energy (E), specific power (P), and the coulombic efficiency (η) values of the symmetrical supercapacitor were calculated from the GCD results using the following equations (1–4).

$$C_{sp}\,(\mathrm{F\ g^{-1}}) = \frac{2I \times \Delta t}{m \times \Delta V} \quad \ldots\ldots\ldots\ldots\ldots\ldots\ (1)$$

$$E\ (\mathrm{Wh\ kg^{-1}}) = \frac{C_s \times \Delta V^2}{28.8} \quad \ldots\ldots\ldots\ldots\ldots\ldots\ldots\ldots\ldots\ldots\ (2)$$

$$P\ (\mathrm{W\ kg^{-1}}) = \frac{E \times 3600}{\Delta t} \quad \ldots\ldots\ldots\ldots\ldots\ldots\ (3)$$

$$\eta = \frac{t_D}{t_C} \times 100\ \% \quad \ldots\ldots\ldots\ldots\ldots\ldots\ldots\ldots\ (4)$$

where, I, Δt, m, and ΔV are defined as the loaded current (A), discharge time (s), loaded mass (g) of active material in each electrode and operating potential range (V), respectively.

2.10 Characterization

The morphology viewpoints were observed by scanning electron microscopy (FESEM, S-4800, Hitachi), and the chemical composition was observed by using energy dispersive x-ray (EDX, TSL, AMETEK) integrated with SEM. Besides, X-ray diffraction (XRD) patterns are recorded in X-ray spectroscopy and used to observe chemical structure, phase, and crystallinity. The proportion of ordered and disordered carbon in the as-prepared ZIF-67-rGO-Mn_xO_y was analyzed by Raman spectroscopy.

References

1. Tarek, Y. A. (2021). Facile synthesis of nano-structured Ni (OH) 2-MnO2-rGO composite VIA gelation method for potential supercapacitor electrode material.
2. Kaur, M., Kaur, H., & Kukkar, D. (2018, May). Synthesis and characterization of graphene oxide using modified Hummer's method. In AIP conference proceedings (Vol. 1953, No. 1, p. 030180). AIP Publishing LLC.
3. Alam, S. N., Sharma, N., & Kumar, L. (2017). Synthesis of graphene oxide (GO) by modified hummers method and its thermal reduction to obtain reduced graphene oxide (rGO). Graphene, 6(1), 1-18.
4. Yu, H., Zhang, B., Bulin, C., Li, R., & Xing, R. (2016). High-efficient synthesis of graphene oxide based on improved hummers method. Scientific reports, 6(1), 1-7.
5. Chen, J., Yao, B., Li, C., & Shi, G. (2013). An improved Hummers method for eco-friendly synthesis of graphene oxide. Carbon, 64, 225-229.
6. Mei, X., Meng, X., & Wu, F. (2015). Hydrothermal method for the production of reduced graphene oxide. Physica E: Low-dimensional Systems and Nanostructures, 68, 81-86.
7. Zhong, G., Liu, D., & Zhang, J. (2018). The application of ZIF-67 and its derivatives: adsorption, separation, electrochemistry and catalysts. Journal of Materials Chemistry A, 6(5), 1887-1899.
8. Sundriyal, S., Shrivastav, V., Kaur, H., Mishra, S., & Deep, A. (2018). High-performance symmetrical supercapacitor with a combination of a ZIF-67/rGO composite electrode and a redox additive electrolyte. ACS omega, 3(12), 17348
9. Zhao, M., Tesfay Reda, A., & Zhang, D. (2020). Reduced graphene oxide/ZIF-67 aerogel composite material for uranium adsorption in aqueous solutions. ACS omega, 5(14), 8012-8022.
10. Shahsavari, M., Mortazavi, M., Tajik, S., Sheikhshoaie, I., & Beitollahi, H. (2022). Synthesis and characterization of GO/ZIF-67 nanocomposite: investigation of catalytic activity for the determination of epinine in the presence of dobutamine. Micromachines, 13(1), 88.
11. Tisha, S. A., Shakil, R., Tarek, Y. A., & Firoz, S. H. (2022). A Facile Synthesis of High Performing MnxOy-Rgo Hybrid Composite for Potential Supercapacitor Application. ECS Transactions, 107(1), 17483.
12. Salahuddin, U., Iqbal, N., Noor, T., Hanif, S., Ejaz, H., Zaman, N., & Ahmed, S. (2021). ZIF-67 derived MnO2 doped electrocatalyst for oxygen reduction reaction. Catalysts, 11(1), 92.

CHAPTER 3

RESULTS AND DISCUSSION

3.1 Strategy of material design and mechanism

In this study, the synthesized nanomaterials are namely ZIF-67, Mn_xO_y, GO, rGO, ZIF-67-rGO, Mn_xO_y-rGO, and ZIF-67-rGO-Mn_xO_y. For a comparative study, the ZIF-67, Mn_xO_y, GO, rGO were individually synthesized by adopting different synthesis approaches and then incorporated with another material to form the ultimate hybrid material. In brief, composite formation is mainly done by adopting simple gel formation and hydrothermal processes. Initially, the idea of synthesizing the ternary hybrid of ZIF-67-rGO-Mn_xO_y was initiated from the synergistic performance of Mn_xO_y-rGO.[1] The incorporation of transitional metal oxide into the rGO layers is inevitably one of the challenging but effective approaches in enhancing the overall performance of the synthesized hybrid prepared from Mn_xO_y.[2] Similarly, the incorporation of a zeolitic framework in the rGO-Mn_xO_y was believed to be a great opportunity in enhancing the electrochemical performance of the ZIF-67-rGO-Mn_xO_y ternary hybrid. Thus, this study attempts to investigate the effect of conductive ZIF-67 and Mn_xO_y in the as-prepared ternary hybrid of ZIF-67-rGO-Mn_xO_y. Herein, the synthesis mechanisms and the routes of forming the composite materials are sequentially described in detail.

On the first attempt, the synthesis procedure started with the synthesis of Mn_xO_y. An exothermic redox reaction is predicted to occur during manganese oxide nanoparticle production. Glycerol, a weak reducing agent, quickly interacts with the strong oxidizing agent $KMnO_4$.[3] Dropwise addition of $KMnO_4$ to glycerol solution, on the other hand, resulted in a dark brown colored gel. The response was extremely quick, taking just 30 minutes to complete, and the entire procedure was carried out in an ambient environment.

$$14KMnO_4\ (s) + 4C_3H_5(OH)_3 \rightarrow 7K_2CO_3\ (s) + 7Mn_2O_3\ (s) + 5CO_2\ (g) + 16\ H_2O$$

The dark brown gel began to form a crosslinking network after being heated on the hotplate at 80°C as shown in Figure 3.1. Although the exact composition of the as-prepared gel network is unclear, it is known from the literature that MnO_4^- reduction is required for gel formation. As

observed in the cross-linked network, manganese oxides coexist with some partially oxidized glycerol particles.[4] The gel's condensation process is thought to result in the formation of manganese oxide nanocrystallites. The calcination procedure was carried out at 700°C to transform the crystalline cross-linked network into pure manganese oxide in a subsequent technique.[5] To achieve the regulated development of crystalline manganese oxide in the final product, the temperature and ramping were adjusted. However, various research has been published in the literature that implies phase transition during the calcination process is an uncontrolled issue.[6] As a result, the finished product has a variety of morphology and phases like MnO_2, Mn_2O_3, Mn_3O_4, and Mn_5O_8. At different temperatures, Matthias et al. observed the synthesis of distinct manganese oxides with different phases.[7] The full transformation of manganese oxide was discovered at 700°C with a 50°C ramping. Because the ramping was set to 10°C in our situation, manganese oxides were expected to coexist in the result. XRD was used to validate the precise morphology of the as-prepared nanoparticles, which will be detailed in a further section.

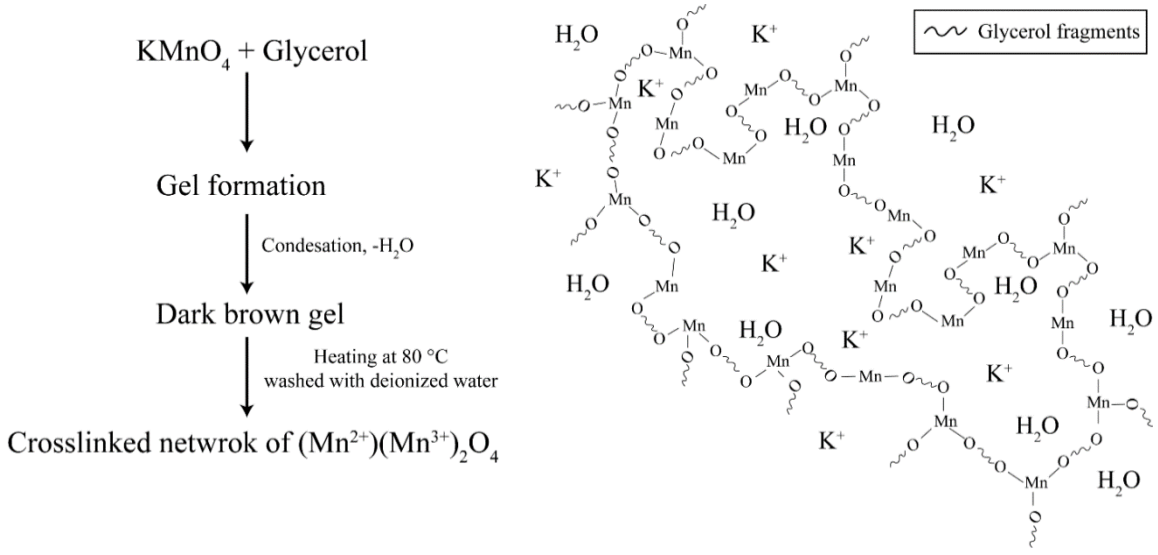

Figure 3.1. Illustration of cross-linking network proposed for (Mn^{2+}, Mn^{3+}) oxides gels[8]

Secondly, solvothermal synthesis using organic liquids, such as N,N-dimethylformamide (DMF) is the most common synthesis technique for ZIF crystals.[9] Qian et al.11 devised and published a ZIF-67 nanocrystals synthesis technique using pure aqueous solutions at room temperature: cobalt nitrate hexahydrate ($Co(NO_3)_2$) and 2-methylimidazole (Hmim) were both dissolved in DI

water.[10] These two solutions were combined and agitated at room temperature, then centrifuged, rinsed with water and methanol, and lastly vacuum-dried to get pure ZIF-67.

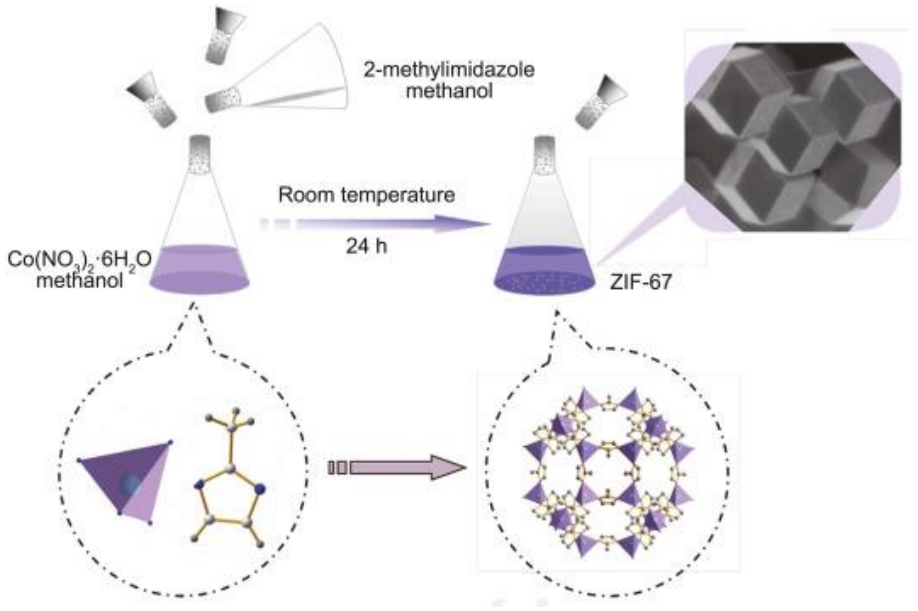

Figure 3.2. Synthesis of ZIF-67 at room temperature.

Three key processes, i.e., hydrolysis, coordination, and deprotonation are generally involved, which makes it easy to precisely control the material properties by changing experimental conditions.[11] But mainly the metal components are bridged by Im (imidazol) linkers in the structure of ZIFs, and the angle M–Im–M is ~145. The structure of the synthesized ZIF-67 is comparable to that of traditional silicon-based zeolites, which is Si–O–Si.[12] Because of their microporous structure, huge surface areas, and adjustable pore aperture, many of them have exceptional thermal and chemical durability.[13] The reaction took place during the formation of the ZIF-67 reaction is followed by,

$$Co(NO_3)_2.6H_2O + C_4H_6N_2 \rightarrow Co(MeIM)_2 + H^+ + NO_3^- + H_2O$$

Organic linkers may exist in two forms during the crystallization: a linker unit in its deprotonated form and a stabilizing unit in its neutral form [14]. Those coexist in the reaction medium at equilibrium. The concentration of deprotonated linker decreases with the pH of the synthesis solution [15]. The decrease in pH stabilizes the neutral linker and then terminates the crystal growth in the synthesis from the fresh solution.

Metal oxides typically prepared are insufficient to fulfill the commercial expectations of energy storage devices in terms of enhancing energy density. The metal oxide was added to ZIF-67 to increase its qualities such as surface area, porosity, and stability, and then carbonaceous materials such as rGO had been added to the composite to improve its cyclability.[16] This rGO was combined directly with the previously synthesized ZIF-67-rGO in the construction of a composite using an ex-situ technique. The ex-situ procedure results have an unexpected outcome. The existing ex-situ composite performance was unsatisfactory. This might be due to the rGO sheet's inherent conductivity being hampered by obstructed nanostructures.[17] The disoriented metal nanoparticle dispersion in the rGO sheets during the ex-situ manufacturing method is defined as the blocked structures. This was an ineffective method for producing a nanoparticle by just combining it with a graphene solution in our situation. The literature has also focused on the in-situ growing creation of metal oxides in the rGO layers to develop hybrid materials for supercapacitors, in addition to the ex-situ procedure.[18]

According to the literature, it is evident that when ZIF-67/TMOs nanostructures are doped with any carbonaceous material, such as GO, rGO, CNT, etc. that helps to improve the characteristics such as surface area, porosity, chemical stability, and thermal stability are enhanced over the pure form.[19] Thus, in this study, the prepared Mn_xO_y and ZIF-67 were individually incorporated with rGO to form the binary composites of rGO-Mn_xO_y and rGO-ZIF-67. During the formation of the rGO-Mn_xO_y, it was found that the concentration of the $KMnO_4$ has played a vital role in the formation of hybrid Mn_xO_y-rGO electrode material.[20] So, a total of two hydrothermal reactions were carried out at 180^oC for 24 hours each with 0.5 mM and 0.5 M $KMnO_4$ to evaluate the concentration influence of $KMnO_4$ on the hydrothermal preparation of rGO-Mn_xO_y composite.[21] It is assumed that upon mixing with the glycerol, the $KMnO_4$ readily reduced into hydrated manganese oxide in the precursor. When the hydrothermal reaction reached 180°C, the available hydroxyl ions supplied the required oxygen to convert the hydrated manganese oxides into the mixture of manganese oxides (Mn_xO_y) and GO into rGO.[22] But, the reason behind the formation of mixed manganese oxides might be caused by the coexistence of cross-linked networks as $(Mn^{2+})(Mn^{3+})_2O_4$. The hydrothermal growth of manganese with 0.5 mM $KMnO_4$ deduced the controlled growth on mixed manganese oxide on and in between the rGO surface.[23] Whereas the reaction with 0.5 M $KMnO_4$ resulted in uncontrolled aggregation of the produced Mn_xO_y throughout the surface of the rGO due to the exaggerated presence of

Mn_xO_y. Hence, after the completion of the reaction, the hybrid synthesized with a lower amount of $KMnO_4$ resulted in an rGO-Mn_xO_y with accessible surface area and channels in between the rGO layers compared to the higher concentration. The possible formation mechanism is shown in Figure 3.3. Following the washing and drying of the obtained materials, electrodes were fabricated, and their behavior in 0.5 M Na_2SO_4 was studied to determine their characteristics.

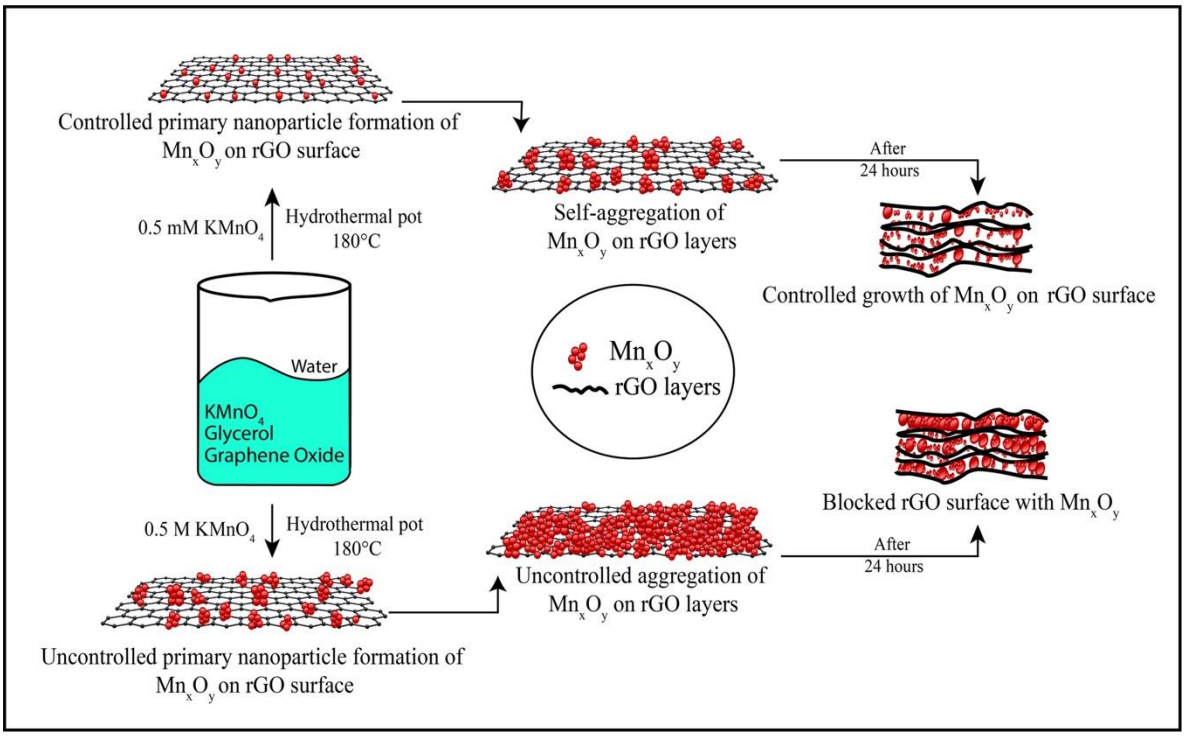

Figure 3.3: Possible formation mechanism of rGO-Mn_xO_y during the hydrothermal reaction.

Similarly, during the formation of ZIF-67-rGO, the formation of polyhedral-shaped ZIF-67 crystals and the conversion of GO to rGO have taken place simultaneously.[24] It is anticipated that when the hydrothermal reaction reached 180^oC, the NO_3^- from the ZIF-67 formation reacts with glycerol ($C_3H_8O_3$) providing enough hydroxyl groups from the reaction which converted the GO into rGO, and during this time the crystal growth of ZIF-67 crystal formation also occurred.[25] But, as the reaction was carried out in a hydrothermal process, it is expected that the polyhedral shape should be distorted due to the excessive pressure and temperature that it should be deposited and grown on the surface of rGO layers.

$$Co(NO_3)_2.6H_2O + C_4H_6N_2 \rightarrow Co(MeIM)_2 + H^+ + NO_3^- + H_2O$$

$$4C_3H_8O_3 + NO_3^- \rightarrow 4C_3H_6O_3 + NH_3 + OH^- + 2H_2O$$

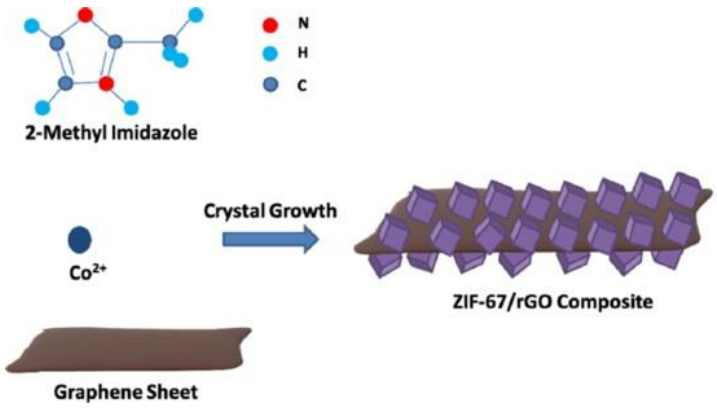

Figure 3.4. Formation mechanism of ZIF-67 on rGO layers during the hydrothermal reaction.

Individually produced rGO from GO was used to compare the electrochemical performance of bare rGO to that of other nanomaterials. The rGO synthesis procedure, on the other hand, was carried out by reducing GO solution by the hydrothermal process at 180°C for 24h.[26] The production of rGO sheets was confirmed by the chemical conversion of brownish GO solution to black gel-like rGO solution. Two different techniques were considered in order to insert several metal oxides into those rGO layers. To begin, an ex-situ mixing procedure was used to combine the rGO nanosheet with the previously manufactured ZIF-67-Mn_xO_y nanoparticles. The ex-situ synthesis procedure was named in fact that it included combining two already produced components in the proximity of the reaction process. The ZIF-67-Mn_xO_y nanoparticles were predicted to be incorporated in between the rGO layers and even on the surface of the rGO layers. Chemically reduced rGO often has a negative zeta potential on its surface, which attracts positively charged cations.[27] The homogeneously distributed rGO was combined in an ex-situ procedure to generate ZIF-67-rGO-Mn_xO_y nanomaterial based on this point. However, due to the strong agglomeration characteristics of rGO layers, ex-situ intercalation of metal oxide nanoparticles in between the rGO layers is relatively inefficient.[28] The permissible interlayer spacing between the rGO layers is reduced once the rGO layers are packed together. As a result, it's quite possible that the integrated metal oxide nanoparticles, rather than interlayers, will cover the exterior rGO surface area. Although any particles made their way into the layers, the proportion should be minimal. As a result of this occurrence, the integrated metal oxides may

block the deficient sides and pores of the bare.[29] On the contrary, using an ex-situ combining procedure to create a hierarchical composite of metal oxides and rGO is nearly impossible.

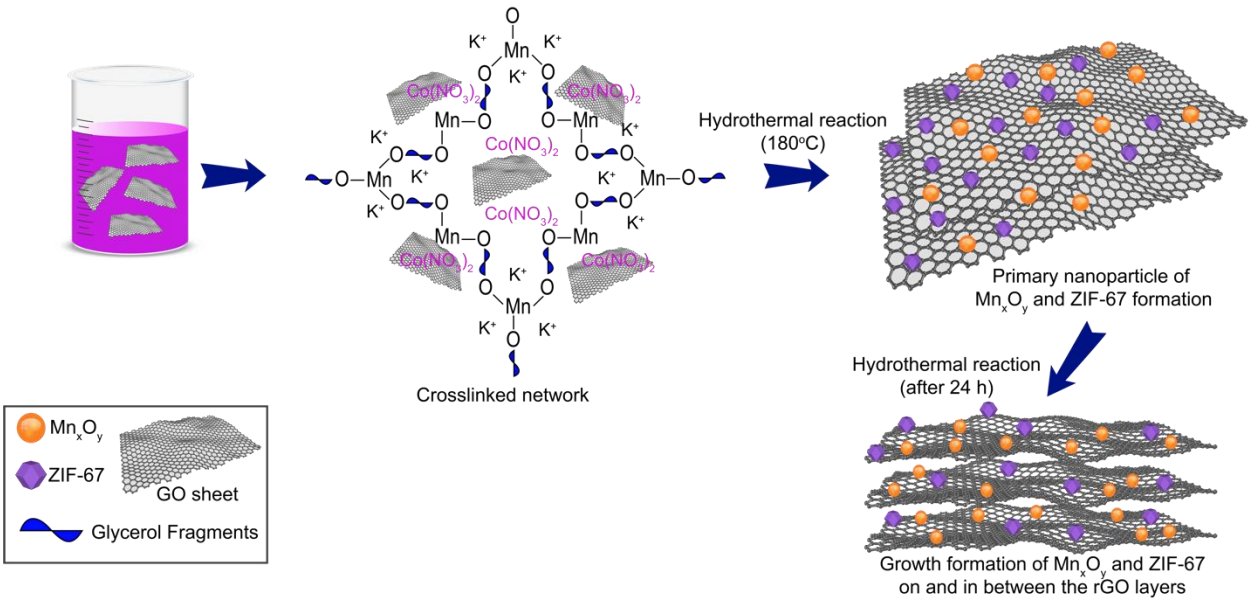

Figure 3.5. Formation mechanism of ZIF-67-rGO-Mn_xO_y during the hydrothermal process.

In order to solve this difficulty, metal oxides or hydroxides are usually suggestive to be included in the rGO layer via an in-situ synthesis technique.[30] The step-by-step mixing of precursors ($KMnO_4$, $Co(NO_3)_2$, and organic linkers) with GO solution was described earlier in section 2.9. When $KMnO_4$ was added to the precursor, immediately hydrated manganese oxide generation via forming a cross-linked network took place.[31] After 1 hour of magnetic stirring, the cobalt nitrate, and the 2-methylimidazol were predicted to be dispersed in the entire cross-linked network as unreacted. During the hydrothermal reaction, Hmim is expected to react with the cobalt nitrate and released NO_3^- as well as produce ZIF-67 crystals right after reaching the reaction at 180°C. The produced NO_3^- then reacted with the excess glycerol and released sufficient OH^-, which is again important for supplying oxygen molecules and converting the hydrated manganese oxide into the desired stable Mn_xO_y. This OH^- is also responsible for converting the GO layers into rGO within the 24h hydrothermal reaction. As the reactions occurred in the interface of rGO layer, the coexistence of ZIF-67 and Mn_xO_y is obvious and thus formed a ternary hybrid of ZIF-67-rGO-Mn_xO_y. The total formation mechanism is presented in Figure 3.5 for better perception.

3.2 Structure, Morphology, and Elemental analysis

3.2.1. Structure, Morphology, and Elemental Analysis

The as-prepared ZIF-67, rGO, Mn_xO_y, and ZIF-67-rGO-Mn_xO_y composite were all analyzed by X-ray diffraction (XRD) to learn more about their atomic structure, crystal structure, and composition. We were able to see that MnO_2 and Mn_2O_3 nanoparticles coexist in the XRD result of pure Mn_xO_y.

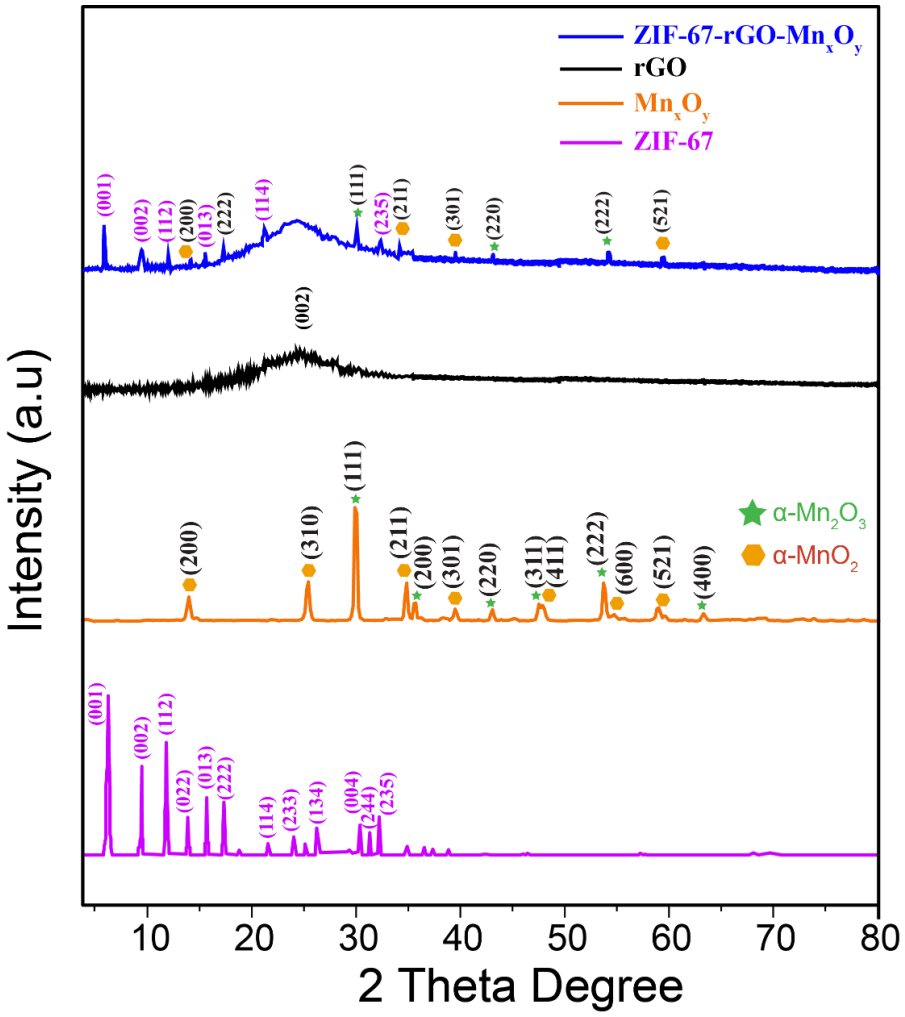

Figure 3.6. XRD diffraction pattern of ZIF-67-rGO-Mn_xO_y, rGO, Mn_xO_y, and ZIF-67.

The pure manganese oxide is shown in Figure 3.6 as Mn_xO_y rather than MnO_2 or Mn_2O_3. Now, the crystals' strong peaks may be seen in the ZIF-67 sample's XRD result. Figure 3.6 displays them, along with the XRD patterns for rGO and the ternary hybrid ZIF-67-rGO-Mn_xO_y. The

statements made about the synthesis techniques can be confirmed by further examination of the XRD patterns, which show the purity and production of the desired product.

The existence of Mn_2O_3 is indicated by the occurrence of peaks at 2 of 32.9°, 38.3°, 45.3°, 49.3°, 55.4°, and 66.2°, which can be indexed as (111), (200), (220), (311), (222), and (400) for Mn_xO_y (JCPDS 41-1442). Additionally, the presence of MnO_2 in the Mn_xO_y was confirmed by peaks at 2 of 12.7°,18.1°,28.8°,37.5°,42.1°,49.9°,56.2°,60.3°, which can be indexed as (110), (200), (310), (211), (301), (411), (600), and (521). It has been discovered that the prepared Mn_xO_y features various phases of manganese oxides, including Mn_2O_3 and MnO_2. Both Mn_xO_y and Mn_2O_3 can be found in their crystalline lattice forms, with MnO_2 having a tetragonal crystal structure and a lattice constant of a = 4.3950, c = 2.8600, and Mn_2O_3 being cubic with a lattice constant of a= 9.41000. hence, pure Mn_xO_y contains multivalent manganese. Again, for ZIF-67, the sodalite nature is evident from the peaks at 2 of 7.53°, 10.56°, and 12.91° for the planes 001, 002, and 112. ZIF-67 is responsible for all the peaks seen at 2, including the ones that arose at energies like JCPDS 61-3852. Characteristic 002 planes at a 2 of 26.2° were seen in the XRD pattern of rGO. The rGO's broader peaks are indicative of its amorphous character.

XRD patterns reveal that ZIF-67-rGO-sharp Mn_xO_y's diffraction peaks can be reliably indexed to JCPDS 38-0734 and the AB stacking order of graphene sheets (10.3°, which corresponds to an interlayer spacing of 0.88 nm). ZIF-67 and Mn_xO_y are included, and their XRD patterns are altered, but at a lower intensity. Light scattering from crystalline ZIF-67 and Mn_xO_y is clearly inhibited by the amorphous rGO layers, however, the presence of the planes 001, 002, 112, 013, 114, and 235 demonstrated that ZIF-67 had been successfully incorporated in between the rGO layers. The inclusion of Mn_xO_y between the rGO layers is also confirmed by the presence of planes 200, 111, 211, 301, 220, 222, and 521. The ZIF-67, MnO_2, and Mn_2O_3 peaks have been seen to move ever-so-slightly, a phenomenon that may have resulted from the simultaneous existence of multiple Mn_xO_y planes.

The morphology of synthesized ZIF-67, GO, rGO, and ZIF-67-rGO-Mn_xO_y, as well as neat Mn_xO_y, was studied using FESEM. Images from a scanning electron microscope (as shown in Figure 3.7) revealed that ZIF-67 has a polyhedral and cube-like shape and measures an average of 80 nm in size. Figure 3.7(b), on the other hand, showed Mn_xO_y to be a capsule-shaped mixed oxide with an average diameter of 72 nm. We used ImageJ to take those readings. Figure 3.7 (c),

on the other hand, demonstrates that agglomerated GO has a smaller conducting surface, making the image unclear.

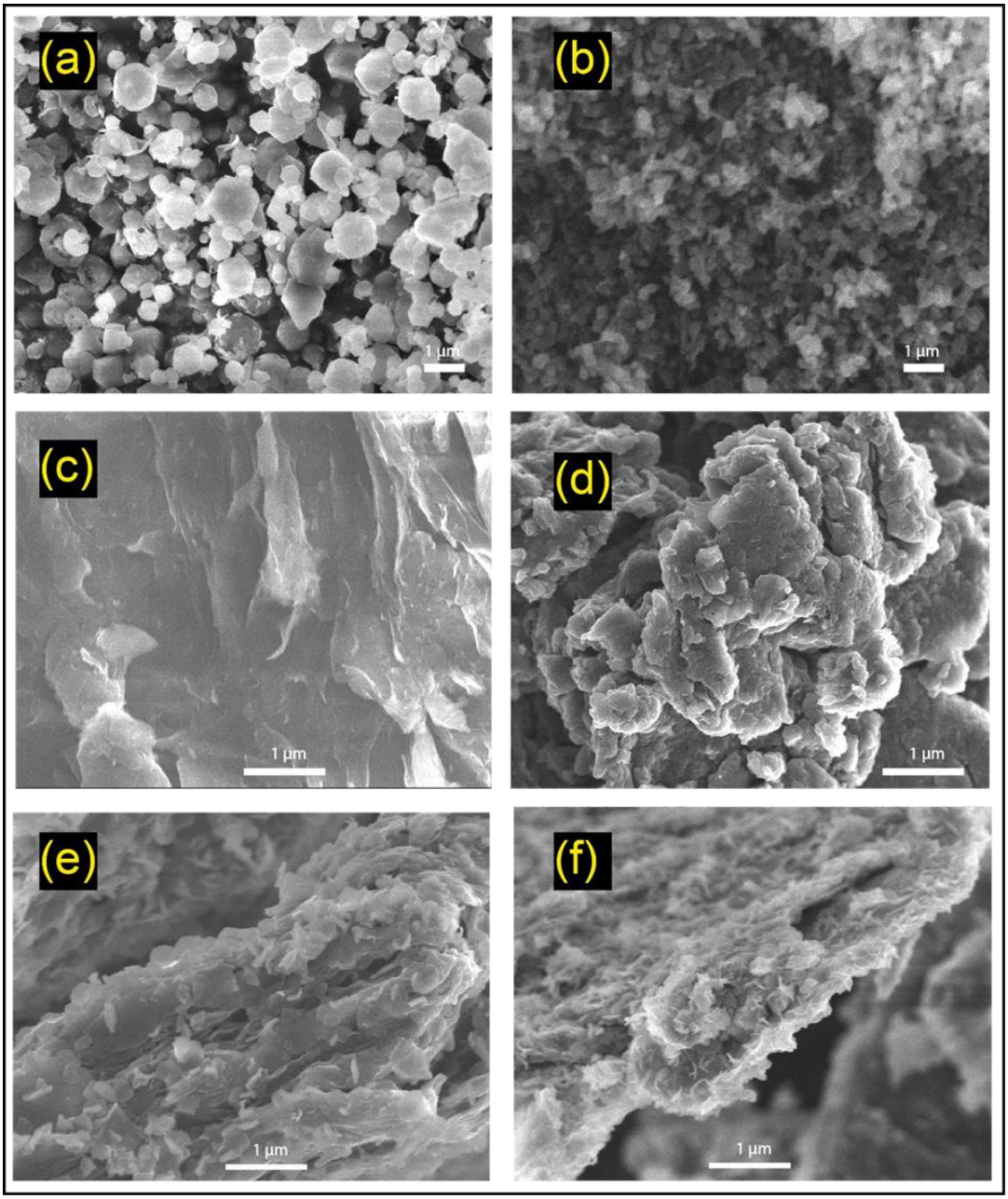

Figure 3.7. SEM images of (a) ZIF-67, (b) Mn_xO_y, (c) GO, (d) rGO, and (e,f) ZIF-67-rGO-Mn_xO_y.

From that vantage point, the GO layer may be seen to be self-stacked. Figure 3.7 (d) shows an SEM picture of rGO, which is much clearer than GO and whose interlayer distance has been

extended in comparison to that of GO. Finally, the surface morphology of rGO has been substantially altered due to the integration of ZIF-67 and Mn_xO_y in between the rGO layer, as shown by the SEM images in Figure 3.7 (e, f). Inside of the entire ZIF-67-rGO-Mn_xO_y hybrid, the shape resembles cornflakes, hence the name stuck.

High-temperature hydrothermal treatment of ZIF-67 with a moderate glycerine agent leads to the production of ZIF-67 and Mn_xO_y. Reducing GO with glycerol at 180° C yields rGO [32]. It's possible that there were three distinct phases of growth formation. Under 180 °C, I glycerol and NO_3^- undertake a redox reaction that releases hydroxyl (OH^-) ions, (ii) Mn^{2+} ions from the cross-linked matrix may react with OH ions to form $Mn(OH)_2$, and (iii) $Mn(OH)_2$ may be transformed to stable Mn_xO_y upon contact with oxygen [33].

The Mn_xO_y primary nanoparticles may disorderly stack with ZIF-67 primary nanocrystals and develop together with rGO to form a hybrid nanosheet due to the hydrogen-bonding interactions between the Mn_xO_y nanoparticles. Figure 3.7 (e,f) shows a scanning electron micrograph showing the assembly of cornflakes with rGO sheets occurring as expected between the rGO layers. These rGO nanosheets tend to cluster in a perpendicular orientation to the surface planes, which lowers the surface energy by decreasing the exposed areas. Therefore, as the reaction continues, the resulting hybrid nanosheets would self-assemble into layered structures in an energy-minimizing manner [34,35].

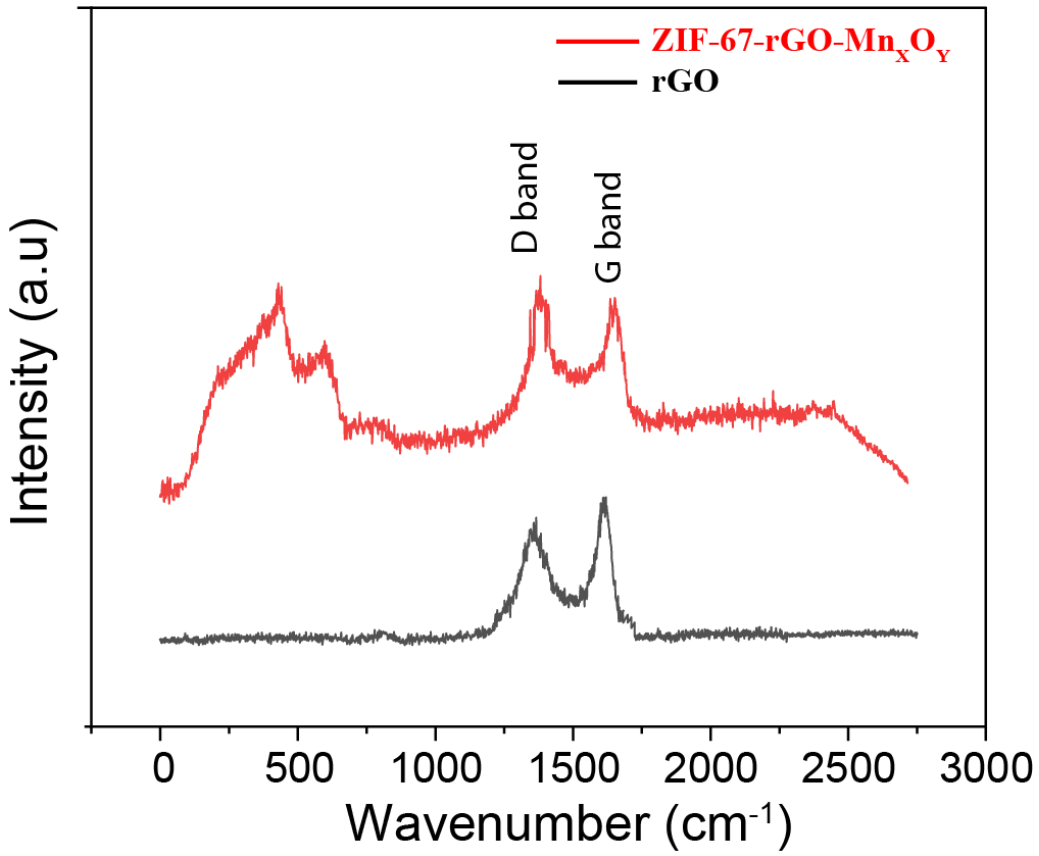

Figure 3.8. Raman spectra of ZIF-67-rGO-Mn_xO_y composite.

The D band represents the disordered structure of graphene whereas the G band represents the planer configuration of the C structure. The D and G bands of the rGO layer can be seen in the Raman spectra of the nanohybrid, at 1337 and 1585 cm^{-1}, respectively (see Figure 3.8 for an example). The stretching vibration of Mn-O and Co-O in Mn_xO_y and ZIF-67 caused the appearance of a second band between 542 and 685 cm^{-1}. The G-band is caused by flaws and disorder in carbon structures, while the D-band is caused by the in-plane vibrations of sp^2-bonded carbon atoms. Defect density and graphitization level can be inferred from the (ID/IG) ratio. The (ID/IG) ratio of 1.25 was due to the extremely wrinkly and curled rGO layers. Graphite flake quality degrades above 1.0, whereas rGO processes become more prevalent below 1.0. Raman spectra of the ternary hybrid and rGO are compared (Figure 3.8), and the intercalation of ZIF-67 and Mn_xO_y increased the ID/IG ratio. The high-temperature hydrothermal process is responsible for this anomaly because it is assumed to have caused a rotational mismatch between the adjacent rGO layers.

3.3.2 Elemental Analysis

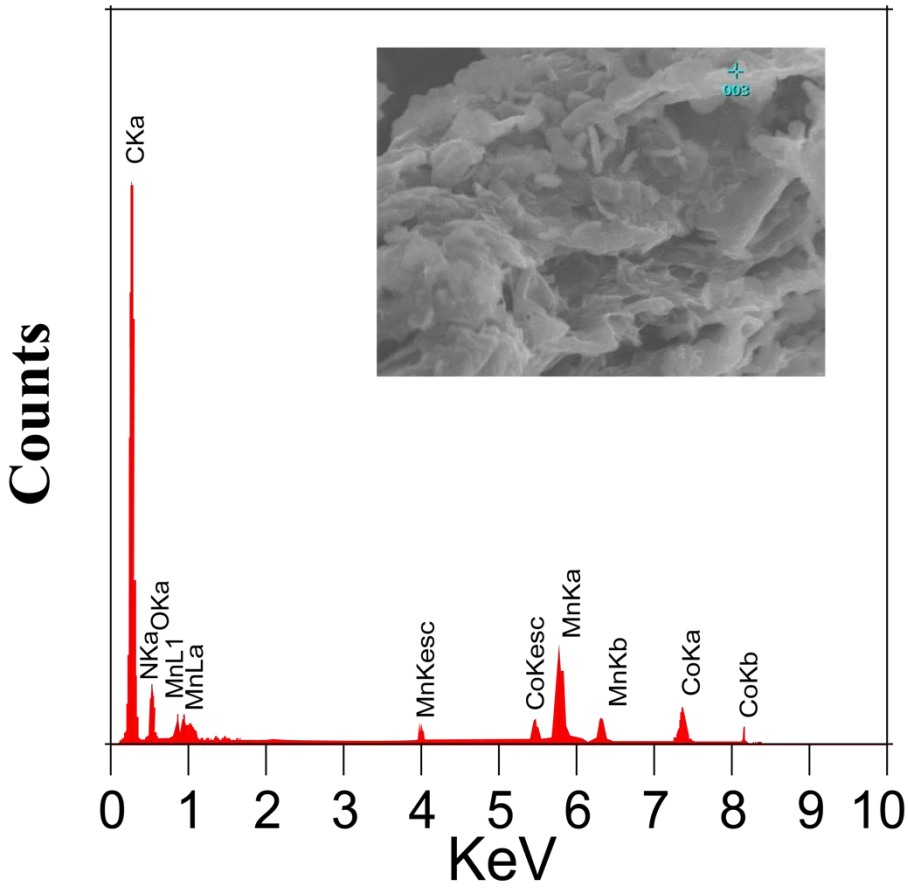

Figure 3.9. EDX spectrum of ZIF-67-rGO-Mn_xO_y composite.

Energy Dispersive X-ray (EDX) has been used to conduct elemental analysis on ZIF-67-rGO-Mn_xO_y nanocomposites. Figure 3.9 shows that the K lines of C, O, Mn, and Co each have maxima at 0.277, 0.523, 5.898, and 8.040 keV. Therefore, the EDX results verify that the necessary components are present in the produced nanocomposites.

Compared to carbon and oxygen, the EDX result for rGO layers showed that the amounts of manganese and nickel were negligible (C = 76% O = 9%, Mn = 11 %, Co= 4%). The purity of the as-prepared ZIF-67-rGO-Mn_xO_y is confirmed by the lack of any unwanted components in the sample. However, the discovery also hints that future studies can experiment with varying the number of metal nanoparticles to see if the composite's performance improves.

3.3 Electrochemical and capacitive performance

3.3.1 Electrochemical Characteristics

In this section, the electrochemical performance of synthesized ZIF-67, Mn_xO_y, GO, rGO, ZIF-67-rGO, rGO-Mn_xO_y, and ZIF-67-rGO-Mn_xO_y are presented. All the calculations regarding the specific capacitance measurement, energy density, and power density calculation are presented before in experimental section. Besides, all the tests were conducted using a neutral 0.5 M Na_2SO_4 electrolyte.

Firstly, the CV and GCD results of manganese oxide are presented in Figure 3.10.1. From the CV curves of Figure 3.10.1. (a), it has been observed that with a different scan rate between 0.0 to +0.7 V, the Mn_xO_y showed different current responses. Most of the time, the higher scan rates show a greater response to current and high specific capacitance. To calculate the C_{sp} of the Mn_xO_y, the GCD performance was undertaken at 1.0, 2.0, and 4.0 Ag^{-1} current density.

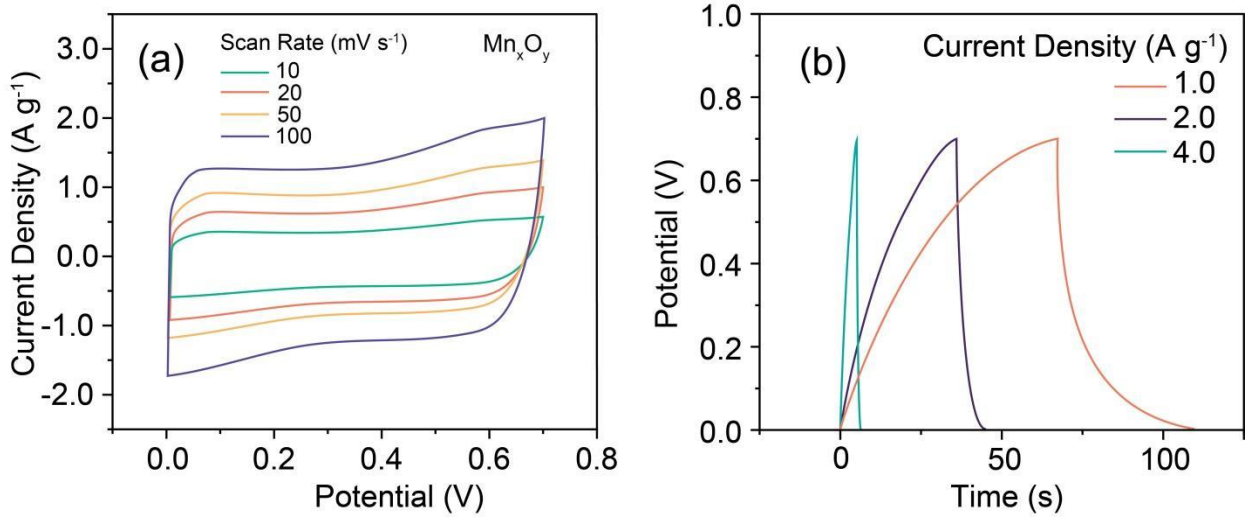

Figure 3.10.1. CV and GCD of Mn_xO_y.

The highest C_{sp} was found to be 85.71 Fg^{-1} at 1 Ag^{-1}, and the energy, as well as power density, were found to be 1.46 $Whkg^{-1}$ and 175.0 Wkg^{-1}, respectively. However, it is well established that Mn_xO_y is prominent for its multivalent oxidation state.[36] During electrochemical redox reactions, the multivalent state makes it easier for the pseudocapacitance to work. A large surface area also helps EDLC form on the part of the electrode that can be reached.[37] Although the

limited working potential provided by Na_2SO_4 is responsible for lower energy density, it is again effective for its higher dielectric constant and provides sufficient conductivity. Considering, the synthesized Mn_xO_y, the specific capacitance is satisfactory, but the inaccessible surface area, as well as uncontrolled morphology, might be responsible for the lower energy density within this limited potential window.

In the second step, the synthesized ZIF-67 was tested. In figure 3.10.2 the detailed CV and GCD of ZIF-67 are depicted. In Figure 3.10.2 (a) different scan rates ranging from 10-100 mVs^{-1} showed different current responses between 0.0 to +0.6 V. The GCD performance was also done using 1.0, 2.0, and 4.0 1 Ag^{-1} current density, and the highest C_{sp} was found to be 73.33 Fg^{-1} at 1 Ag^{-1} for ZIF-67. The energy and power density was also calculated and those are 0.92 $Whkg^{-1}$ and 150 Wkg^{-1} respectively. However, compared to the Mn_xO_y, the overall current response in CV curves of ZIF-67 was found to be lower and that indicates the uncalcined ZIF-67 is not reactive and the accessible surface is not available towards the electrolyte ions. Thus, a lesser current response and lesser specific capacitance have been found. However, to overcome the problem regarding both the Mn_xO_y and ZIF-67, both were incorporated with rGO as it can provide more channels and accessible active surfaces with much higher conductivity.[38] But, before that, the electrochemical performance of both GO and rGO was tested for the comparative study.

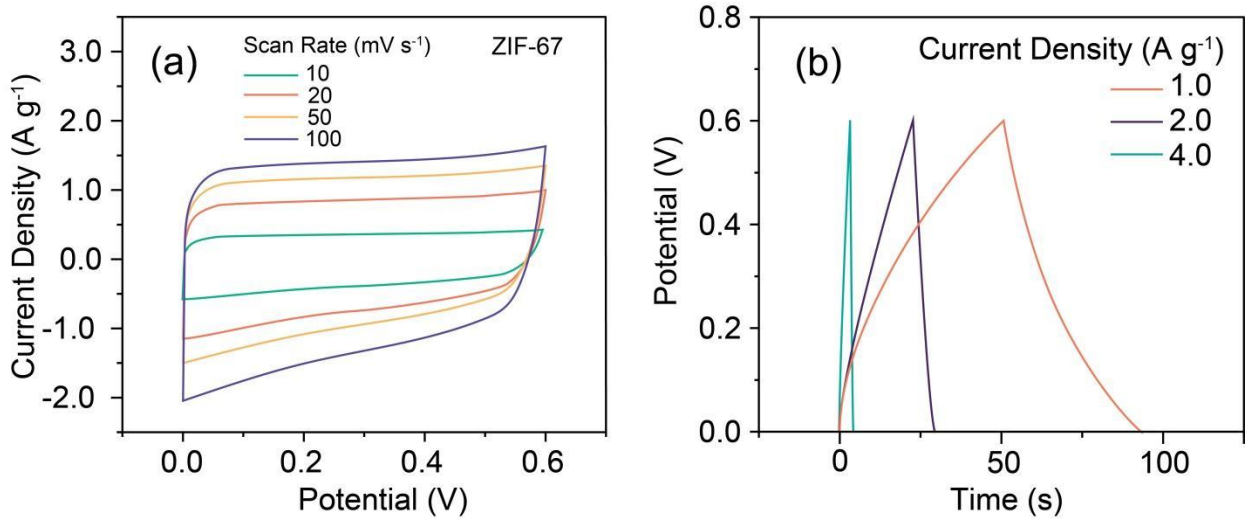

Figure 3.10.2. CV and GCD of ZIF-67.

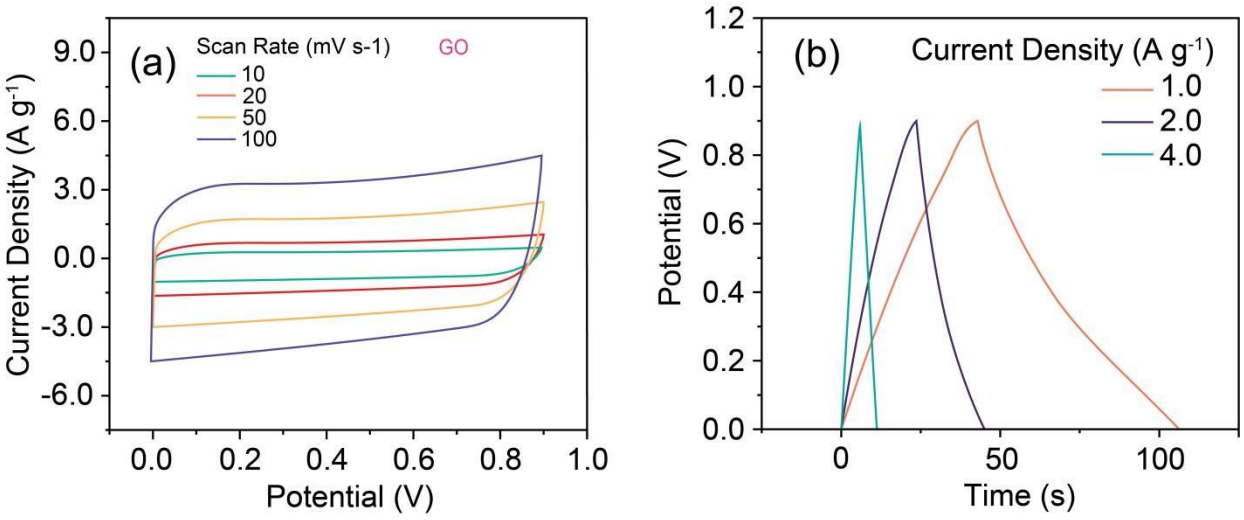

Figure 3.10.3. CV and GCD of GO.

In Figure 3.10.3. and 3.6.4, the CV and GCD results of GO and rGO are presented, respectively. By observing the CV curves of both GO and rGO, it is noticeable that the current response of rGO has far better than that GO at all scan rates. Besides, the CV curves of the rGO shapes become more rectangular, which makes it ideal for an electrical double-layer capacitor.[39] That is again proved by measuring the Csp of both GO and rGO. From the GCD calculation, it was found that GO exhibited a specific capacitance of 97.78 Fg^{-1} with an energy density of 2.75 $Whkg^{-1}$ and power density of 225.0 Wkg^{-1} at 1 Ag^{-1} current density. On the contrary, rGO exhibited a specific capacitance of 266.67 Fg^{-1} with an energy density of 7.50 $Whkg^{-1}$ and power density of 225.0 Wkg^{-1} at 1 Ag^{-1} current density. Those comparative results indicated that rGO is attributed to higher conductivity and larger surface area, which is more accessible to the electrolytes of Na_2SO_4. Thus, even within the working potential (0-+0.9V), the rGO has achieved more energy density without compromising any power density.

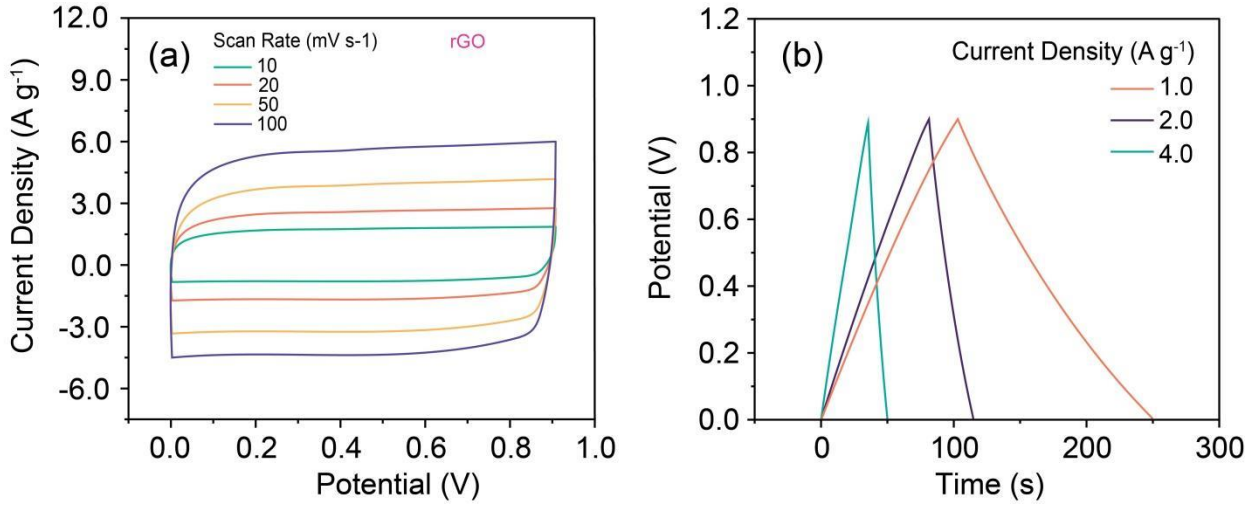

Figure 3.10.4. CV and GCD of rGO.

The initial choice was to combine carbonaceous elements like rGO with metal oxides. Usually, rGO is incorporated by both in-situ and ex-situ methods. But, according to most of the literature, it has been found that ex-situ incorporation is always ineffective as the incorporation of external material in the rGO layers during the synthesis procedure is much more difficult than inserting them in the in-situ process[40]. However, based on this point of view, both the Mn_xO_y and ZIF-67 were incorporated in the rGO layers by adopting an in-situ process and tested against the same electrolyte.

The properties like surface area, porosity, cyclability, chemical, and thermal stability of modified ZIF-67 are improved by the incorporation of rGO [41]. Usually, the expanded window is provided by an extra surface area which means a large amount of charge accumulation occurs during the electrochemical charging process. From Figure 3.10.5 (a), it is visible that the current responses in CV curves have enhanced compared to ZIF-67 alone. Besides, the area under the CV curves indicated a better accessible surface area. After incorporating rGO with ZIF-67, the window for ZIF-67-rGO was found to be 0.0 to +1.2 V, where specific capacitance was found to be 325.00 Fg^{-1} at $1Ag^{-1}$ using 0.5M Na_2SO_4. Whereas the working potential was only limited to (0-+0.7V) for the bare ZIF-67. The energy density of this composite was found 16.25 $Whkg^{-1}$ with a power density of 300 Wkg^{-1}. Herein, we can see that the successful incorporation of rGO increases the surface area, overall conductivity, and electrochemical performance of ZIF-67-rGO composite.

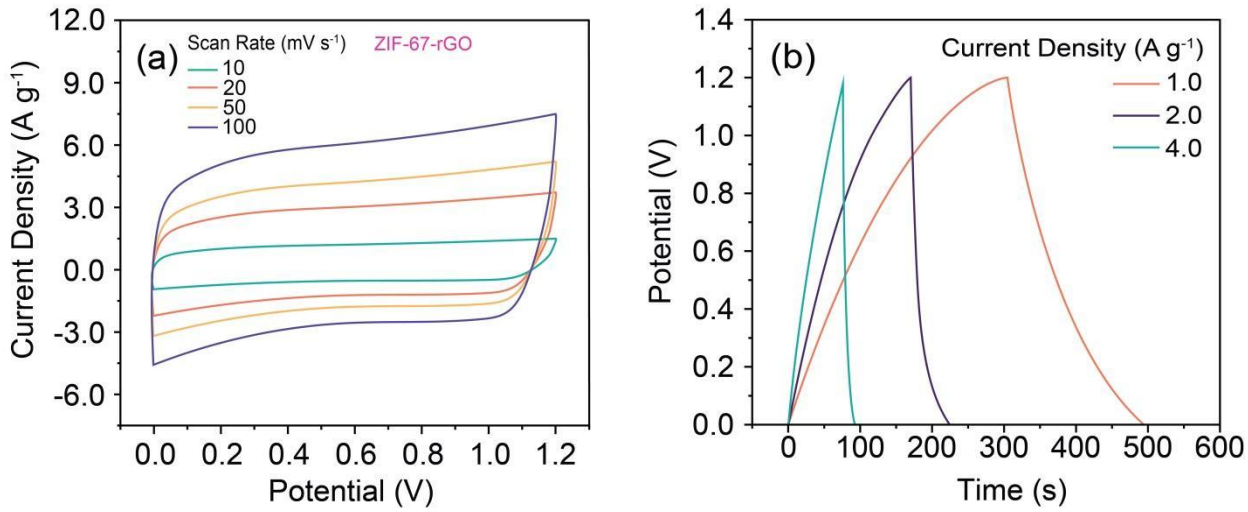

Figure 3.10.5. CV and GCD of ZIF-67-rGO.

To observe the effect of MnxOy in between the rGO layers, the Mn_xO_y-rGO composite was also synthesized and the electrochemical performance was evaluated. In Figure 3.10.6. the CV curves and GCD curves for rGO-$Mn_xO_y$is are presented. Likewise, ZIF-67-rGO composite, the synergistic effect of another material with rGO was also observed for rGO-Mn_xO_y and found that the rGO-Mn_xO_y has shown better current responses in CV curves compared to bare Mn_xO_y.

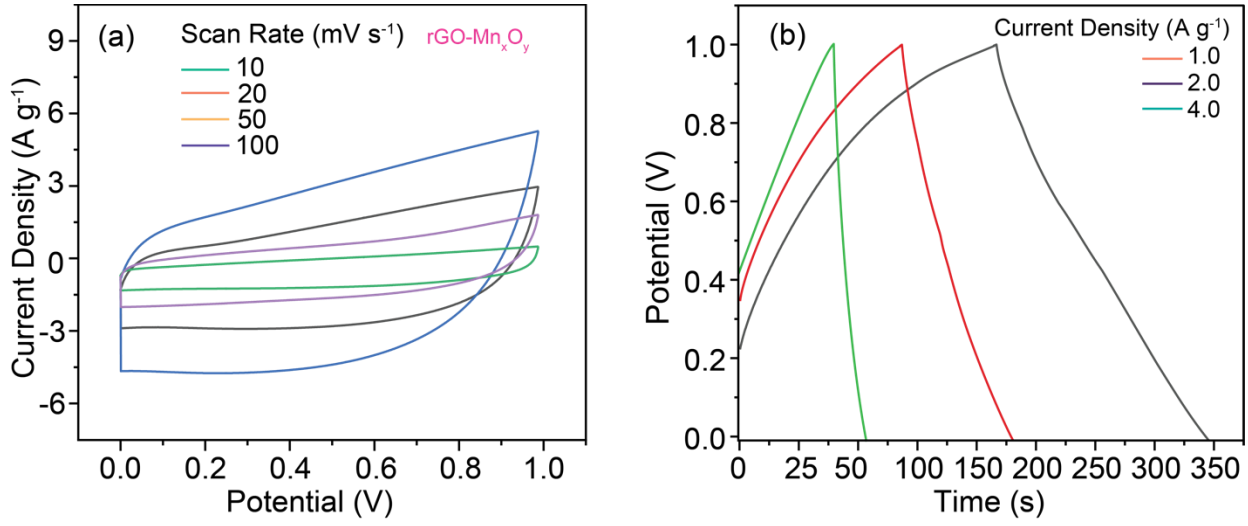

Figure 3.10.6. CV and GCD of Mn_xO_y-rGO.

The window expansion between 0.0 to +1.0 V using 0.5 M Na_2SO_4 electrolytes. As a result, from the GCD results of Figure 3.10.6 (b), it has been found that the specific capacitance was found

280.00 Fg^{-1} at $1Ag^{-1}$ where energy density was calculated to be 9.72 $Whkg^{-1}$ with a power density of 250.00 Wkg^{-1} at 1 Ag^{-1} current density.

The hydrothermal growth of ZIF-67 and Mn_xO_y in the rGO layers during in-situ inclusion resulted in ZIF-67-rGO-Mn_xO_y. In Figure 3.11. (a), the CV curves for ZIF-67-rGO-Mn_xO_y have been presented. It has been seen that the current response and the area under the curve have expanded more than any other synthesized materials in this study. The result of CV curves was as expected because the synergistic effect of both Mn_xO_y and ZIF-67 contributed to the ternary hybrid of ZIF-67-rGO-Mn_xO_y. However, observing the GCD curves of Figure 3.11 (b), the effect of the incorporation of that individual entity, can be observed. The specific capacitance of ZIF-67-rGO-Mn_xO_y was determined to be the highest 457.14 Fg^{-1} at 1 Ag^{-1}. The energy density and power density of ZIF-67-rGO-Mn_xO_y were found 31.11 $Whkg^{-1}$ and 350 Wkg^{-1} at 1 Ag^{-1} current density. The surface area and interlayer spacing between rGO layers is increased by the self-oriented growth development of ZIF-67 and Mn_xO_y. The production of metal oxides facilitates the self-assembly of rGO layers that are closer together. This nanostructure is favorable for counter electron flow when a potential difference is implemented. For the composite of ZIF-67-rGO-Mn_xO_y, a potential window of 1.4 V was obtained, as shown in Figure 3.11 (c). The formation of granular-shaped self-oriented ZIF-67 and Mn_xO_y capsules, which allow aggregating sufficient charge inside a broad window while preserving excellent conductivity and mobility, may have caused the window to expand.

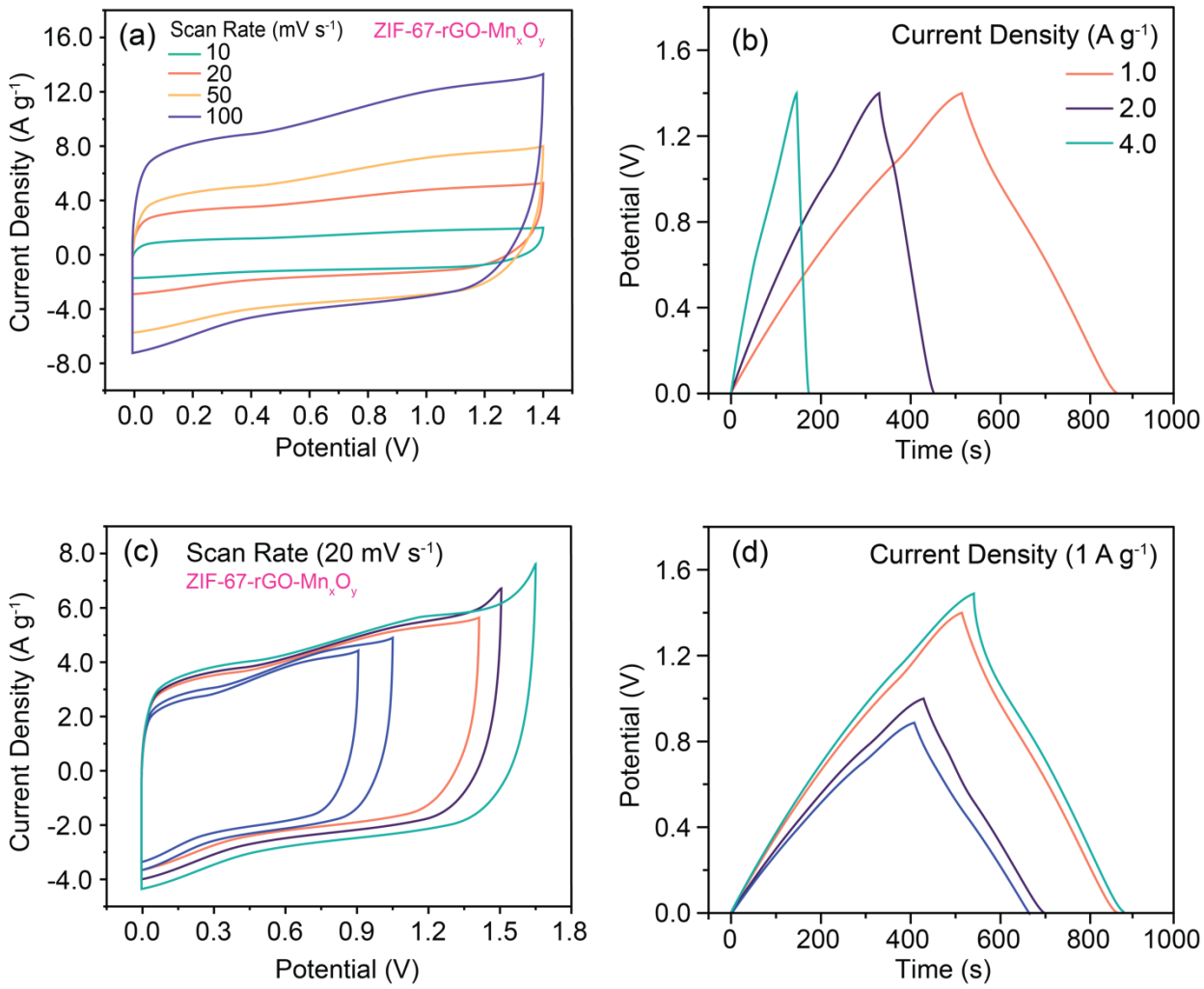

Figure 3.11. (a) CV of ZIF-67-rGO-Mn_xO_y composite at different scan rates (b) GCD of ZIF-67-rGO-Mn_xO_y composite at different current density (c) determination of effective working potential window for ZIF-67-rGO-Mn_xO_y, and (d) verification of the potential window using GCD.

The electrochemical performance of all the synthesized materials was performed using 0.5 M Na_2SO_4 electrolyte and showed in Figure 3.12. In figure 3.2 (a) the CV curve of all synthesized materials (ZIF-67-rGO-Mn_xO_y, ZIF-67-Mn_xO_y, ZIF-67-rGO, Mn_xO_y-rGO, rGO, GO, Mn_xO_y, ZIF-67) is shown at a scan rate of 20 mVs^{-1}. From the comparison of this study, it can be declared that the current response of ZIF-67-rGO-Mn_xO_y is maximum compared to the others as well as the working potential is also improved compared to the other materials. The perfect

rectangular shape indicates the best EDLC layer formation during the electrochemical reactions.[42]

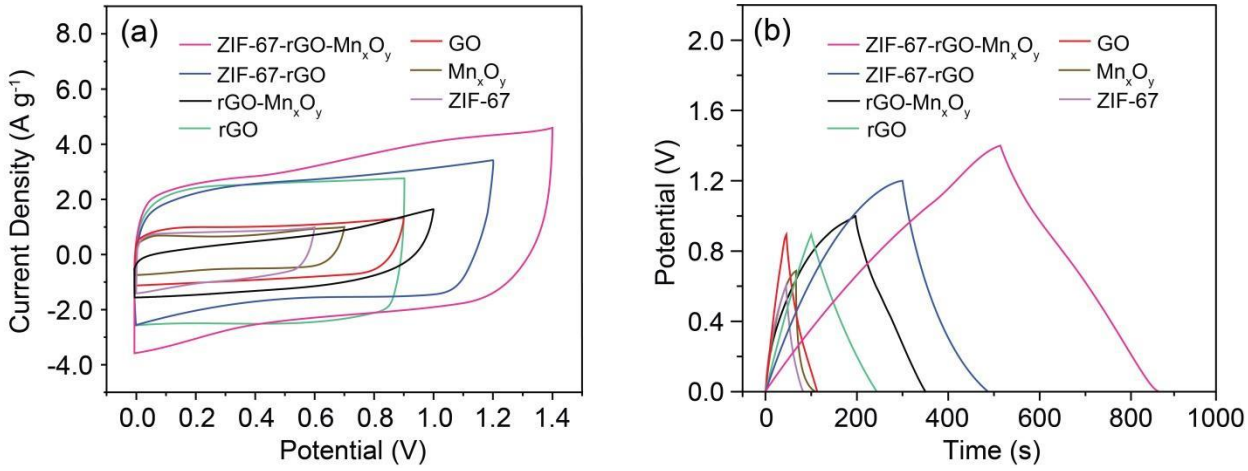

Figure 3.12. (a) Comparison of CV curve of ZIF-67-rGO-Mn_xO_y, ZIF-67-rGO, rGO-Mn_xO_y, rGO, GO, Mn_xO_y, ZIF-67. (b) Comparison of GCD curve of ZIF-67-rGO-Mn_xO_y, ZIF-67-rGO, rGO-Mn_xO_y, rGO, GO, Mn_xO_y, ZIF-67.

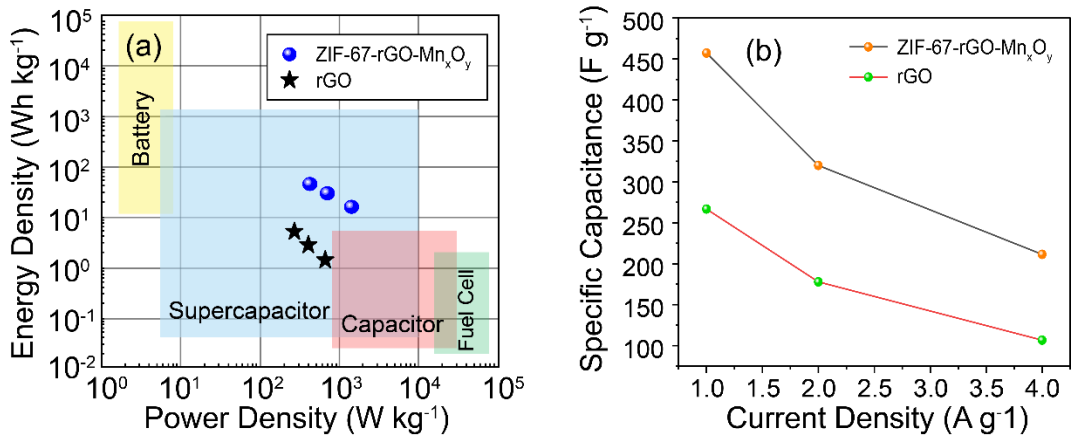

Figure 3.13. (a) Ragone plot for the comparison of the supercapacitor performance of the synthesized materials. (b) Variation of specific capacitance with various current densities.

The energy density vs. power density comparison has been shown in figure 3.13 (a). From this research, it is established that the ZIF-67-rGO-Mn_xO_y hybrid composite has accomplished the properties necessary for a competent supercapacitor material. And can be seen in figure 3.13 (b) that the specific capacitance drops dramatically as the current density changes, but it is

noticeable that the performance rate of the synthesized ternary hybrid has not decreased significantly even upon applying high current density. These findings show that ZIF-67-rGO-Mn_xO_y is a competitive supercapacitor material.

Table 3.1. Summary of the electrochemical results of ZIF-67, Mn_xO_y, GO, rGO, Mn_xO_y-rGO, ZIF-67-rGO, ZIF-67-rGO-Mn_xO_y.

Materials	***Current Density, Ag^{-1}***	***Specific Capacitance, Fg^{-1}***	***Energy Density, $Whkg^{-1}$***	***Power Density, Wkg^{-1}***
ZIF-67	1.0	73.33	0.92	150.00
	2.0	53.33	0.67	300.00
	4.0	26.67	0.33	600.00
Mn_xO_y	1.0	85.71	1.46	175.00
	2.0	51.43	0.88	350.00
	4.0	45.71	0.78	700.00
GO	1.0	97.78	2.75	225.00
	2.0	75.56	2.13	450.00
	4.0	53.33	1.50	900.00
rGO	1.0	266.67	7.50	225.00
	2.0	177.78	5.00	450.00
	4.0	106.67	3.00	900.00
rGO-Mn_xO_y	1.0	280.00	9.72	250.00
	2.0	200.00	6.94	500.00
	4.0	99.00	3.33	1000.00
ZIF-67-rGO	1.0	325.00	16.25	300.00
	2.0	183.33	9.17	600.00
	4.0	86.67	4.33	1200.00
ZIF-67-rGO-Mn_xO_y	1.0	**457.14**	**31.11**	350.00
	2.0	320.00	21.78	700.00
	4.0	211.43	14.39	1400.00

3.3.2 Impedance analysis

An electrochemical impedance spectrometer (EIS) produces Nyquist plots that look like a clear semicircle at high frequencies and a straight line at low frequencies. R_s (ohmic resistance) from the electrolyte, electrode material, and various other possible ohmic resistances between the working electrode can be characterized using the intercept of the semicircle at the real axis (Z').[43] The electrochemical impedance of (ZIF-67-rGO-Mn_xO_y, ZIF-67-Mn_xO_y, ZIF-67-rGO, Mn_xO_y-rGO, rGO, GO, Mn_xO_y, ZIF-67) electrodes was investigated in 0.5 M Na_2SO_4 across the frequency range of (105 to 0.01) Hz. On the other hand, ZIF-67-rGO-Mn_xO_y exhibits the lowest solution resistance values (as shown in Figure 3.14). The R_s and R_{ct} values for all materials are listed in Table 3.2. R_s is the value of this composite material. When it comes to manganese oxides, Mn_xO_y has the greatest solution resistance value because it has the lowest conductivity and the highest wettability at the solid electrolyte contact.[44] It's decreased solution resistanceis probably due to it's hybrid nanostructure of ZIF-67-rGO-Mn_xO_y.

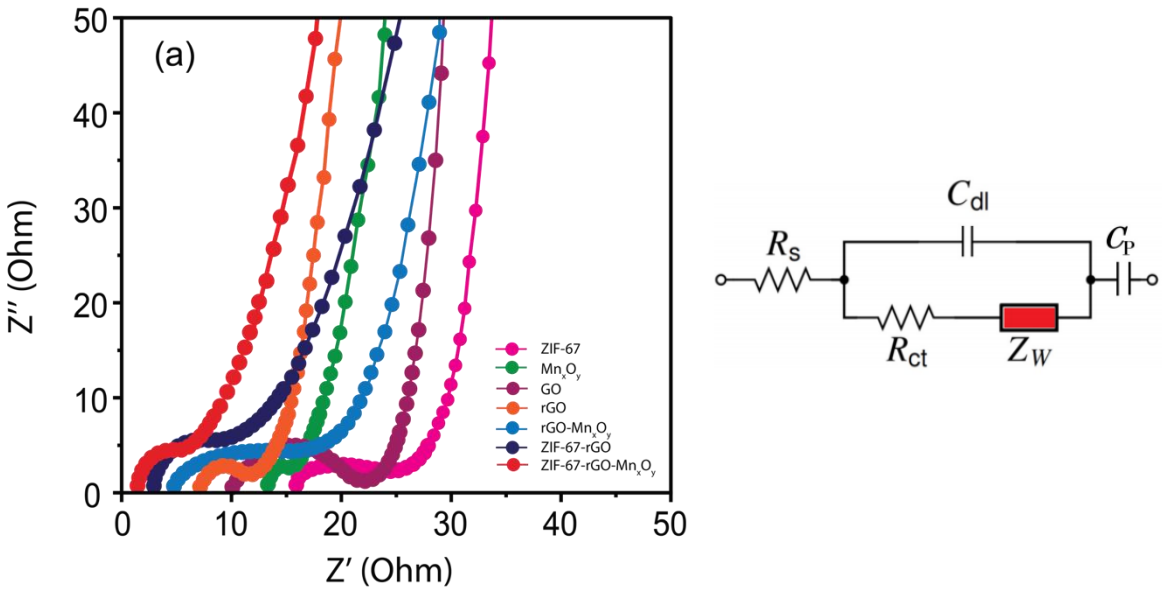

Figure. 3.14. EIS of ZIF-67-rGO-Mn_xO_y, ZIF-67-rGO, rGO-Mn_xO_y, rGO, GO, Mn_xO_y, ZIF-67 with circuit fitting.

When pseudocapacitive nanoparticles are deposited on top of the rGO layer, a surprising synergy is generated, which boosts the electrode's conductivity. As a result, the ZIF-67-rGO-Mn_xO_y

hybrid composite was found to have the lowest charge transfer resistance (R_{ct}) of any of the materials tested, at 8.5. Redox interactions between the electrode and electrolyte cause a charge transfer resistance (abbreviated as R_{ct}) that grows in proportion to the semicircle's diameter [45]. It's because an increase in the specific surface area decreases the distance traveled by active ions. Warburg impedance, as demonstrated by Z [46], is proportional to the slope of a straight line.

Table 3.2. Summary of the R_s and R_{ct} values for the synthesized nanomaterials.

Unit	**Mn_xO_y**	**ZIF-67**	**ZIF-67-rGO**	**rGO-Mn_xO_y**	**ZIF-67-rGO-Mn_xO_y**
R_s(Ω)	13.8	15.2	3.9	5.2	2.3
R_{ct} (Ω)	48.2	32.6	24.5	16.6	8.5
C_{dl} (μF)	7.84×10^{-6}	3.78×10^{-5}	1.32×10^{-5}	1.58×10^{-4}	2.9×10^{-2}
C_p (μF)	0.00825	0.00675	0.03522	0.01654	0.03021
W (cm^2/s)	0.00875	0.00921	0.00672	0.00765	0.00523

The diffusion rate of the stored and released active ions during charging and discharging can be described using this value. The circuit elements' double-layer capacitance (C_{dl}) and pseudocapacitance (C_p) are represented by C_{dl} and C_p, respectively. Fitting the RC circuit shows that ZIF-67-rGO-Mn_xO_y is the best-produced nanomaterial when using 0.5 M Na_2SO_4 as the electrolyte.

3.2.3 Cyclic Stability

When we talk about the cyclic stability (or electrochemical cyclic stability) of electrode material, we're referring to the ongoing study of its electrochemical performance, such as its initial capacitance retention and coulombic efficiency under the working potential with a high current density.[47]

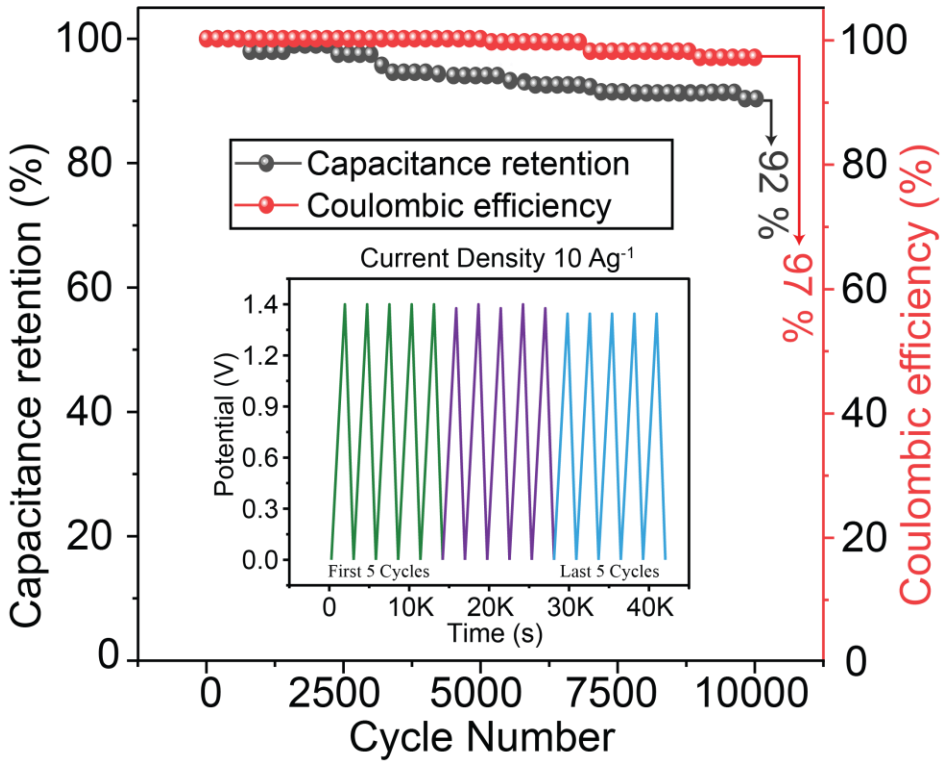

Figure. 3.15. Cyclic stability test of ZIF-67-rGO-Mn_xO_y composite at a current density of 10 Ag^{-1}.

Once again, the ratio of discharge to charge capacity during the same cycle is the Coulombic efficiency (η). The stability of the ZIF-67-rGO-Mn_xO_y-based device was evaluated by cycling it through 2000 GCD cycles at a fixed current density of 10 Ag^{-1} in a symmetric cell containing 0.5 M Na_2SO_4. The voltage was varied from 0.0 to 1.0 V. Figure 3.15 shows the device stability as the change of coulombic efficiency as a function of the number of cycles. ZIF-67-rGO-Mn_xO_y electrode samples in 0.5 M Na_2SO_4 electrolytes maintained 97% of their initial coulombic efficiency after 10000 cycles. In a neutral electrolyte solution, the multilayer structure of ZIF-67-rGO-Mn_xO_y underwent a little modification. It was an indication of how long the material will last. Neutral electrolytes are preferred because they do not damage the electrode materials during the electrochemical process [48,49]. The high percentage of coulombic efficiency was also attributed to the easy and highly accessible interconnected layers that facilitate retaining stability after a long cycle of the ZIF-67-rGO-Mn_xO_y. The capacitance retention and coulombic efficiency were calculated using equations (6) and (7) respectively.

$$\text{Capacitance retention} = \frac{n^{th}\ \text{cycle capacitance}}{1^{st}\ \text{cycle capacitance}} \times 100\ \% \qquad (6)$$

$$\text{Coulombic efficiency, } \eta = \frac{t_{discharge}}{t_{charge}} \times 100\% \qquad (7)$$

The first five cycles had a coulombic efficiency of 100%, retaining 100% of the capacitor's capacitance, while the latter five cycles had a coulombic efficiency of 97%, retaining 90% of the capacitor's capacitance. Since the electrolyte ions can travel freely without disrupting the nanostructures, the well-defined, stable layered structure may be responsible for the highly retainable capacitance performance. This finding hints at the as-prepared ZIF-67-rGO-Mn_xO_y composite's potential long-term utility in the construction of a real-time supercapacitor.

References

1. Ali, G. A., Yusoff, M. M., Algarni, H., & Chong, K. F. (2018). One-step electrosynthesis of MnO2/rGO nanocomposite and its enhanced electrochemical performance. Ceramics International, 44(7), 7799-7807.
2. Lei, Z., Lee, J. M., Singh, G., Sathish, C. I., Chu, X., Ala'a, H., ... & Yi, J. (2021). Recent advances of layered-transition metal oxides for energy-related applications. Energy Storage Materials, 36, 514-550.
3. Tarek, Y. A. (2021). Facile synthesis of nano-structured Ni (OH) 2-MnO2-rGO composite VIA gelation method for potential super capacitor electrode material.
4. Padayachee, D., Golovko, V., & Marshall, A. T. (2013). The effect of MnO2 loading on the glycerol electrooxidation activity of Au/MnO2/C catalysts. Electrochimica Acta, 98, 208-217.
5. Augustin, M., Fenske, D., Bardenhagen, I., Westphal, A., Knipper, M., Plaggenborg, T., ... & Parisi, J. (2015). Manganese oxide phases and morphologies: A study on calcination temperature and atmospheric dependence. Beilstein journal of nanotechnology, 6(1), 47-59.
6. Amirsalari, A., & Shayesteh, S. F. (2015). Effects of pH and calcination temperature on structural and optical properties of alumina nanoparticles. Superlattices and Microstructures, 82, 507-524.
7. Augustin, M., Fenske, D., Bardenhagen, I., Westphal, A., Knipper, M., Plaggenborg, T., ... & Parisi, J. (2015). Manganese oxide phases and morphologies: A study on calcination temperature and atmospheric dependence. Beilstein journal of nanotechnology, 6(1), 47-59.
8. Ullah, A. A., Kibria, A. F., Akter, M., Khan, M. N. I., Maksud, M. A., Jahan, R. A., & Firoz, S. H. (2017). Synthesis of Mn3O4 nanoparticles via a facile gel formation route and study of their phase and structural transformation with distinct surface morphology upon heat treatment. Journal of Saudi Chemical Society, 21(7), 830-836.
9. Chen, Y., & Tang, S. (2019). Solvothermal synthesis of porous hydrangea-like zeolitic imidazole framework-8 (ZIF-8) crystals. Journal of Solid State Chemistry, 276, 68-74.
10. Oar-Arteta, L., Wezendonk, T., Sun, X., Kapteijn, F., & Gascon, J. (2017). Metal organic frameworks as precursors for the manufacture of advanced catalytic materials. Materials Chemistry Frontiers, 1(9), 1709-1745.

11. Duan, C., Yu, Y., & Hu, H. (2020). Recent progress on synthesis of ZIF-67-based materials and their application to heterogeneous catalysis. Green Energy & Environment.
12. Feng, Y., Wang, H., & Yao, J. (2021). Synthesis of 2D nanoporous zeolitic imidazolate framework nanosheets for diverse applications. Coordination Chemistry Reviews, 431, 213677.
13. Duan, C., Yu, Y., & Hu, H. (2020). Recent progress on synthesis of ZIF-67-based materials and their application to heterogeneous catalysis. Green Energy & Environment.
14. Şahin, F., Topuz, B., & Kalıpçılar, H. (2018). Synthesis of ZIF-7, ZIF-8, ZIF-67 and ZIF-L from recycled mother liquors. Microporous and Mesoporous Materials, 261, 259-267.
15. Huelsenbeck, L., Luo, H., Verma, P., Dane, J., Ho, R., Beyer, E., ... & Giri, G. (2020). Generalized approach for rapid aqueous MOF synthesis by controlling solution pH. Crystal Growth & Design, 20(10), 6787-6795.
16. Zaman, N., Iqbal, N., & Noor, T. (2022). Comparative study of Mn-ZIF-67 derived carbon (Mn-Co/C) and its rGO-based composites for the methanol oxidation. Journal of Environmental Chemical Engineering, 10(5), 108351.
17. Sun, Y., & Shi, G. (2013). Graphene/polymer composites for energy applications. Journal of Polymer Science Part B: Polymer Physics, 51(4), 231-253.
18. Jung, J., Jeong, J. R., Lee, J., Lee, S. H., Kim, S. Y., Kim, M. J., ... & Lee, M. H. (2020). In situ formation of graphene/metal oxide composites for high-energy microsupercapacitors. NPG Asia Materials, 12(1), 1-9.
19. Zhuang, G. L., Gao, Y. F., Zhou, X., Tao, X. Y., Luo, J. M., Gao, Y. J., ... & Wang, J. G. (2017). ZIF-67/COF-derived highly dispersed Co3O4/N-doped porous carbon with excellent performance for oxygen evolution reaction and Li-ion batteries. Chemical Engineering Journal, 330, 1255-1264.
20. Tarek, Y. A., Reaz, A. H., Shakil, R., Roy, H., Jahan, R. A., Roy, C. K., & Firoz, S. H. (2020, December). One-Step Gel Formation Method for the Synthesis of NiO-Mn X O Y Mixed Oxide Nanomaterials as a Prospective Supercapacitor Material. In 2020 2nd International Conference on Sustainable Technologies for Industry 4.0 (STI) (pp. 1-6). IEEE.
21. Tisha, S. A., Shakil, R., Tarek, Y. A., & Firoz, S. H. (2022). A Facile Synthesis of High Performing MnxOy-Rgo Hybrid Composite for Potential Supercapacitor Application. ECS Transactions, 107(1), 17483.

22. Dessie, Y., Tadesse, S., Eswaramoorthy, R., & Abebe, B. (2019). Recent developments in manganese oxide based nanomaterials with oxygen reduction reaction functionalities for energy conversion and storage applications: A review. Journal of Science: Advanced Materials and Devices, 4(3), 353-369.
23. Qiu, G., Huang, H., Dharmarathna, S., Benbow, E., Stafford, L., & Suib, S. L. (2011). Hydrothermal synthesis of manganese oxide nanomaterials and their catalytic and electrochemical properties. Chemistry of Materials, 23(17), 3892-3901.
24. Sundriyal, S., Shrivastav, V., Kaur, H., Mishra, S., & Deep, A. (2018). High-performance symmetrical supercapacitor with a combination of a ZIF-67/rGO composite electrode and a redox additive electrolyte. ACS omega, 3(12), 17348-17358.
25. Kharisov, B. I., & Kharissova, O. V. (2019). Less-common carbon nanostructures. In Carbon Allotropes: Metal-Complex Chemistry, Properties and Applications (pp. 111-302). Springer, Cham.
26. Hidayat, R., Wahyuningsih, S., & Ramelan, A. H. (2020, June). Simple synthesis of rGO (reduced graphene oxide) by thermal reduction of GO (graphene oxide). In IOP Conference Series: Materials Science and Engineering (Vol. 858, No. 1, p. 012009). IOP Publishing.
27. Li, M. J., Liu, C. M., Cao, H. B., & Zhang, Y. (2013). Surface charge research of graphene oxide, chemically reduced graphene oxide and thermally exfoliated graphene oxide. In Advanced Materials Research (Vol. 716, pp. 127-131). Trans Tech Publications Ltd.
28. Norizan, M. N., Abdullah, N., Halim, N. A., Demon, S. Z. N., & Mohamad, I. S. (2022). Heterojunctions of rGO/Metal Oxide Nanocomposites as Promising Gas-Sensing Materials—A Review. Nanomaterials, 12(13), 2278.
29. Ellis, B. L., Knauth, P., & Djenizian, T. (2014). Three-dimensional self-supported metal oxides for advanced energy storage. Advanced Materials, 26(21), 3368-3397.
30. Li, Z., Wang, R., Wu, S., Xue, Z., Zhu, D., Zou, J., & Li, X. (2021). In situ observation of metal ion interactions with graphene oxide layers: From the growth of metal hydroxide to metal oxide formation. Carbon, 184, 721-727.
31. Shevchenko, D., Anderlund, M. F., Styring, S., Dau, H., Zaharieva, I., & Thapper, A. (2014). Water oxidation by manganese oxides formed from tetranuclear precursor complexes: the influence of phosphate on structure and activity. Physical Chemistry Chemical Physics, 16(24), 11965-11975.

32. Wang, X., Salari, M., Jiang, D. E., Chapman Varela, J., Anasori, B., Wesolowski, D. J., ... & Gogotsi, Y. (2020). Electrode material–ionic liquid coupling for electrochemical energy storage. Nature Reviews Materials, 5(11), 787-808.
33. Zhao, M., Tesfay Reda, A., & Zhang, D. (2020). Reduced graphene oxide/ZIF-67 aerogel composite material for uranium adsorption in aqueous solutions. ACS omega, 5(14), 8012-8022.
34. Gao, Q., Giraldo, O., Tong, W., & Suib, S. L. (2001). Preparation of nanometer-sized manganese oxides by intercalation of organic ammonium ions in synthetic birnessite OL-1. Chemistry of materials, 13(3), 778-786.
35. Boles, M. A., Engel, M., & Talapin, D. V. (2016). Self-assembly of colloidal nanocrystals: From intricate structures to functional materials. Chemical reviews, 116(18), 11220-11289.
36. Wang, Y., He, J., Liu, C., Chong, W. H., & Chen, H. (2015). Thermodynamics versus kinetics in nanosynthesis. Angewandte Chemie International Edition, 54(7), 2022-2051.
37. Franchini, C., Podloucky, R., Paier, J., Marsman, M., & Kresse, G. (2007). Ground-state properties of multivalent manganese oxides: Density functional and hybrid density functional calculations. Physical Review B, 75(19), 195128.
38. Du, X., Guo, P., Song, H., & Chen, X. (2010). Graphene nanosheets as electrode material for electric double-layer capacitors. Electrochimica Acta, 55(16), 4812-4819.
39. Ansari, A. R., Ansari, S. A., Parveen, N., Ansari, M. O., & Osman, Z. (2021). Silver nanoparticles embedded on reduced graphene Oxide@ Copper oxide nanocomposite for High Performance Supercapacitor Applications. Materials, 14(17), 5032.
40. Torad, N. L., Salunkhe, R. R., Li, Y., Hamoudi, H., Imura, M., Sakka, Y., ... & Yamauchi, Y. (2014). Electric double-layer capacitors based on highly graphitized nanoporous carbons derived from ZIF-67. Chemistry–A European Journal, 20(26), 7895-7900.
41. Sundriyal, S., Shrivastav, V., Kaur, H., Mishra, S., & Deep, A. (2018). High-performance symmetrical supercapacitor with a combination of a ZIF-67/rGO composite electrode and a redox additive electrolyte. ACS omega, 3(12), 17348-17358.
42. Singh, V. K., Patra, M. K., Manoth, M., Gowd, G. S., Vadera, S. R., & Kumar, N. (2009). In situ synthesis of graphene oxide and its composites with iron oxide. New carbon materials, 24(2), 147-152.

43. Senthilkumar, S. T., Selvan, R. K., Ponpandian, N., Melo, J. S., & Lee, Y. S. (2013). Improved performance of electric double layer capacitor using redox additive (VO 2+/VO 2+) aqueous electrolyte. Journal of Materials Chemistry A, 1(27), 7913-7919.
44. Hernández, H. H., Reynoso, A. M. R., González, J. C. T., Morán, C. O. G., Hernández, J. G. M., Ruiz, A. M., ... & Cruz, R. O. (2020). Electrochemical impedance spectroscopy (EIS): A review study of basic aspects of the corrosion mechanism applied to steels. Electrochemical Impedance Spectroscopy, 137-144.
45. Hu, Y., Wu, Y., & Wang, J. (2018). Manganese-oxide-based electrode materials for energy storage applications: how close are we to the theoretical capacitance?. Advanced Materials, 30(47), 1802569.
46. Sun, J. J., Zhao, H. Z., Yang, Q. Z., Song, J., & Xue, A. (2010). A novel layer-by-layer self-assembled carbon nanotube-based anode: Preparation, characterization, and application in microbial fuel cell. Electrochimica Acta, 55(9), 3041-3047.
47. Funabiki, A., Inaba, M., Ogumi, Z., Yuasa, S. I., Otsuji, J., & Tasaka, A. (1998). Impedance study on the electrochemical lithium intercalation into natural graphite powder. Journal of the Electrochemical Society, 145(1), 172.
48. Wu, Q., He, T., Zhang, Y., Zhang, J., Wang, Z., Liu, Y., ... & Ran, F. (2021). Cyclic stability of supercapacitors: materials, energy storage mechanism, test methods, and device. Journal of Materials Chemistry A.
49. Huang, S., Zhu, J., Tian, J., & Niu, Z. (2019). Recent progress in the electrolytes of aqueous zinc-ion batteries. Chemistry–A European Journal, 25(64), 14480-14494.

CHAPTER 4

CONCLUSIONS AND FUTURE ASPECTS

4.1 Conclusion

The gel formation method was successfully adopted in the synthesis of ZIF-67-rGO-Mn_xO_y. Its surface morphology and nanostructure are found to be unique due to the successful incorporation of Mn_xO_y, and ZIF-67 in rGO surface. The composite showed a high C_{sp} of 457.14 Fg^{-1} at 1 Ag^{-1} in 0.5M Na_2SO_4 electrolyte, along with a high energy density (31.11$Whkg^{-1}$) and a power density (350.0 Wkg^{-1}). The enhanced performance as a supercapacitor can be attributed to the synergistic interaction between ZIF-67 and Mn_xO_y in rGO layers, which helps to enhance strong ion intercalation and overall conductivity. The colombic effenciency is found 97% even after 10000 cycles at 10 Ag^{-1} current density. From these overall work it can be decleared that a hybrid supercapacitivr material has been synthesized successfully. The Result from this study will help improve the manufacturing process for supercapacitor materials, which in turn will aid in the introduction of green technology in the energy storage industry.